Petroleum Science 22 (2025) 977–997

Contents lists available at ScienceDirect

Petroleum Science

journal homepage: www.keaipublishing.com/en/journals/petroleum-science

Original Paper

Water adsorption performance of over-mature shale and its relationship with organic and inorganic nanopores: A case study of Lower Cambrian shale from the Sichuan Basin, China

Yi-Jie Xing [a], Xian-Ming Xiao [a, b, *], Peng Cheng [c], Yan-Ming Zhao [a], Wei Liu [a]

[a] School of Energy Resources, China University of Geosciences (Beijing), Beijing, 100083, China
[b] Frontiers Science Center for Deep-time Digital Earth, China University of Geosciences (Beijing), Beijing, 100083, China
[c] Guangzhou Institute of Geochemistry, Chinese Academy of Sciences, Guangzhou, 510640, Guangdong, China

ARTICLE INFO

Article history:
Received 15 March 2024
Received in revised form
18 June 2024
Accepted 26 December 2024
Available online 30 December 2024

Edited by Jie Hao

Keywords:
Lower cambrian shale
Over-mature
Water vapor adsorption
Organic pores
Inorganic pores

ABSTRACT

The water adsorption performance of shale gas reservoirs is a very important factor affecting their gas in place (GIP) contents, but the water-holding capacity and mechanism of over-mature shale, especially organic pores, are still not fully understood. In this study, systematic water vapor adsorption (WVA) experiments were carried out on the Lower Cambrian over-mature shale and its kerogen from the Sichuan Basin, China to characterize their WVA behaviors, and combined with the low-pressure gas (N_2 and CO_2) adsorption experiments, the main influencing factors of WVA capacity of the shale and the absorbed-water distribution in its organic and inorganic nanopores were investigated. The results show that the WVA isotherms of shale and kerogen are all type II, with an obvious hysteresis loop in the multilayer adsorption range, and that the positive relationship of the shale TOC content with the WVA capacity (including total adsorption capacity, primary adsorption capacity and secondary adsorption capacity) and WVA hysteresis index (AHIW), and the greater adsorption capacity and AHIW of kerogen than the shale, all indicate that the hydrophilicity of organic matter (OM) in the over-mature shale was underestimated in previous research. Although both the shale OM and clay minerals have a significant positive effect on the WVA, the former has a stronger adsorption ability than the latter. The WVA capacity of the studied Lower Cambrian shale is significantly greater than that of the Longmaxi shale reported in literatures, which was believed to be mainly attributed to its higher maturity, with a significant graphitization of OM. The shale micropores and non-micropores play an important role in WVA, especially OM pores. There are primary and secondary adsorption for water vapor in both the micropores and non-micropores of OM, while these adsorptions of minerals mainly occur in their non-micropores. These results have important guides for understanding the gas storage mechanism and exploration and development potential of marine over-mature shale in southern China, especially the Lower Cambrian shale.

1. Introduction

With the breakthrough and application of technologies such as horizontal drilling and hydraulic fracturing, shale gas, as an important replacement energy source, has be effectively developed. In the recent decade, China has vigorously promoted the exploration of the Lower Paleozoic (Upper Ordovician Wufeng Formation-Lower Silurian Longmaxi Formation; Lower Cambrian) marine shale gas in its south area, and a great progress has been made in the Wufeng-Longmaxi formations in the Sichuan Basin and its surrounding areas (Zou et al., 2015; Dong et al., 2016). In 2022, the shale gas production arrived to 223.23 × 10^8 m^3 in the Sichuan Basin (Yang et al., 2023), accounting for 93% of the total shale gas production (240 × 10^8 m^3) and 10% of the total natural gas production (2201.1 × 10^8 m^3) in China (Dong et al., 2022; Nie et al., 2022). However, the gas content of Lower Cambrian shale is generally lower than that of the Wufeng-Longmaxi formations, and the gas content and tested productivity vary widely in different

* Corresponding author.
E-mail address: xmxiao@cugb.edu.cn (X.-M. Xiao).

https://doi.org/10.1016/j.petsci.2024.12.025

regions (Wang et al., 2014, 2016a; Zhang et al., 2023). The Lower Cambrian shale gas has not yet been developed commercially.

Shale reservoirs contain a certain amount of water. For example, the water content of marine shale gas reservoirs in southern China is generally between 10% and 60%, and can reach 90% in some blocks (Curtis, 2002; Liu and Wang, 2013; Fang et al., 2014; Zou et al., 2015; Ren et al., 2019). Water in shale is an important factor affecting shale gas content and production (Hu et al., 2019; Khan et al., 2021; Feng et al., 2023; Xing et al., 2023). For gas-bearing shale, the actual pore water saturation is much lower than the theoretical irreducible water saturation, and it is in an ultra-low water saturation (Cheng et al., 2018; Bai et al., 2020). Under this case, the water is basically bound state, i.e., it is adsorbed in the shale nanopores through the forms of water film, cluster and condensation (Fang et al., 2014; Yu et al., 2021; Dang et al., 2021). Water in shale occupies some pore spaces and adsorption sites, which can significantly reduce the contents of free gas and adsorbed gas (Jin and Firoozabadi, 2014; Li et al., 2016, 2019a; Wu et al., 2017). On the other hand, in the process of hydraulic fracturing development, a portion of the fracturing water will remain in shale reservoirs, which is benefit to gas desorption (Parmar et al., 2013; You et al., 2021). Therefore, understanding the water adsorption mechanism and occurrence in shale reservoirs is of great significance to the exploration and development of shale gas.

In recent years, water vapor adsorption (WVA) has been widely used to study the adsorption performance of water in shale (Zolfaghari et al., 2017b; Sang et al., 2019, 2020; Wang et al., 2019b; Yang et al., 2020a; Dang et al., 2021; Ukaomah et al., 2023), and combined with the characterization technology of shale nanopore structure (such as low-pressure gas adsorption experiments), this method gets a deep understanding on the controlling factors of water adsorption in shale (Sang et al., 2018; Yang et al., 2020a; Chen et al., 2021a). The previous research shown that the water vapor adsorption behavior in shale is influenced by various factors, including clay minerals, brittle minerals, total organic carbon (TOC) content, thermal maturity, pore structure characteristics, as well as some external factors (such as temperature and pressure) (Feng et al., 2018; Yang et al., 2020a; Chen et al., 2021a; Li et al., 2021a; Shi et al., 2023). Clay mineral and organic matter (OM) are the main carriers of water in shale (Li et al., 2019b; Zhu et al., 2020), and their water vapor adsorption characteristics are significantly different. Clay minerals have strong hydrophilicity (Zolfaghari et al., 2017a; Sang et al., 2019; Lahn et al., 2020), and water vapor can be adsorbed on clay minerals by van der Waals forces, hydrogen bonds, capillary forces, electrostatic forces, surface hydration and cation exchange (Osipov, 2012; Hou et al., 2021; Song et al., 2022). Because of the different understanding of hydrophilicity or hydrophobicity of OM in shale, it is still controversial whether OM pores can adsorb water. Some studies suggest that hydrocarbons mainly exist in kerogen pores, and there is almost no water in OM pores (Heller and Zoback, 2014; Feng et al., 2018). However, the hydrophobicity of OM will change with its thermal maturation evolution (Hu et al., 2015, 2016). The higher the thermal maturity, the more the nanopores and the less the hydrophilic groups (e.g., carboxyl and hydroxyl groups). Obviously, the increase of nanopores is beneficial to the hydrophilicity of OM, while the reduction of hydrophilic groups is not conducive to the hydrophilicity of OM. Despite of this, OM pores still have water storage capacity even at a very high maturity level (Kuila et al., 2014; Gu et al., 2016; Cheng et al., 2017, 2018; Xing et al., 2024). Some porous organic materials without hydrophilic groups (e.g., graphene) have also been found to be mildly hydrophilic (Kozbial et al., 2014; Wei and Jia, 2015), but the mechanism remains unclear.

The adsorption mechanism of water in shale can be analyzed based on the adsorption-desorption isotherms of water vapor (Llave et al., 2012; Arthur et al., 2016; Wan et al., 2016; Shen et al., 2018). These isotherms are often associated with a hysteresis loop, and their morphology is related to pore structure and pore wall hydrophilicity (Zolfaghari et al., 2017b; Chen et al., 2020; Ukaomah et al., 2023). Although available data reveals a stronger relationship between clay minerals and WVA capacity (Wang et al., 2019b), and a relationship also exists between TOC content and hysteresis loop variability (Yang et al., 2020a), it is still not clear how much water is located in OM and inorganic pores (predominantly clay-hosted pores). This is crucial because the difference of wettability properties between OM and inorganic minerals will directly affect the adsorption behavior of water vapor (Chen et al., 2021a). In addition, at present, most of the studies aim at shale, with few studies on kerogen, which may ignore the importance of water uptake of OM in shale.

The current study on the WVA of marine shale in southern China mostly aims at the Longmaxi shale (Duan and Li, 2018; Wang et al., 2019b; Bai et al., 2020; Yang et al., 2020a; Dang et al., 2021; Xie et al., 2023), without reports on the Lower Cambrian shale, and the properties of the two shales are quite different (Ma et al., 2015; Wang et al., 2016b, 2018a). Compared with the Longmaxi shale, the Lower Cambrian shale has a greater maturity, with an equivalent vitrinite reflectance (EqRo) mainly between 3.0% and 5.0%, and the OM in shale samples from the Sichuan Basin and its surrounding areas has an obvious carbonization (i.e., graphitization) (Huang et al., 2012; Wang et al., 2014; Xu et al., 2017; Jiang et al., 2018). The WVA results from the Longmaxi shale cannot be completely applied to the Lower Cambrian shale.

Therefore, in this study, water vapor and low-pressure gas (N_2 and CO_2) adsorption experiments were carried out on the Lower Cambrian over-mature shale and its kerogen from the Weiyuan area, Sichuan Basin, China. Based on the quantitative characterization of the WVA behavior of the shale and kerogen, the influencing factors of the WVA capacity of the shale was investigated and the difference of WVA capacity from the Longmaxi shale reported in literatures were emphatically compared. On the basis of this, the occurrence and distribution characteristics of adsorbed water in the organic and inorganic pores of the shale were discussed.

2. Geological background

The Sichuan Basin, with a total area of about 19×10^4 km^2, is located in the northwest of the Yangtze Platform (Hao et al., 2013; Guo and Zhang, 2014). The basin developed its rudiment in the Indosinian period and formed its present tectonic pattern during the Himalayan period (Shen et al., 2007). A large-scale transgression occurred in the Early Cambrian, and a part of the Sichuan Basin, including the Weiyuan area, and its nearby north and east areas were in the deep water shelf environment (Jiang et al., 2012; Li et al., 2013, 2022a; Cheng et al., 2016; Ren et al., 2017) (Fig. 1), and deposited the Qiongzhusi Formation black shale under the anoxic bottom-water conditions (Pi et al., 2013; Xu et al., 2019; Gao et al., 2021; Li et al., 2022b).

The Weiyuan area is located in the southwestern of the central uplift belt of Sichuan Basin. The Lower Cambrian Qiongzhusi Formation shale in this area has a current burial depth of 2270–4300 m, and a thickness of 400–600 m with a stable distribution (Sui, 2017). The shale has a TOC content of 0.31%–4.89%, and an EqVRo value of 2.6%–4.0%, and the kerogen belongs to type I or II_1 (Wang et al., 2013a; Zhou et al., 2014; Ren et al., 2016, 2017; Sui, 2017; Tian et al., 2018), thus with shale gas exploration potential. According to the data from Ren et al. (2016), shale gas was detected in the Qiongzhusi Formation from 19 wells out of 20 wells in Weiyuan area, and industrial shale gas production was obained

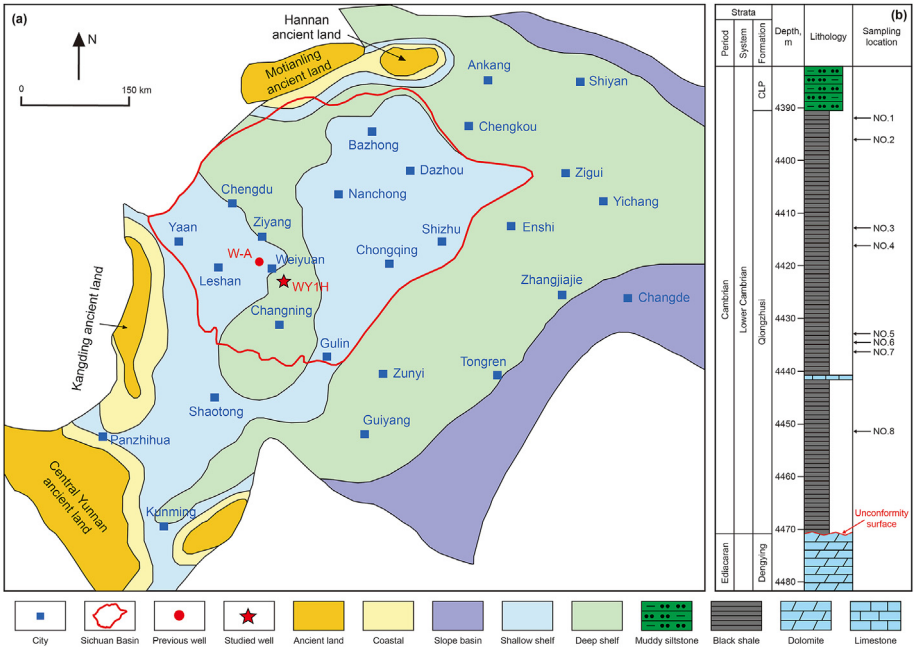

Fig. 1. **(a)** Paleogeographic map of the Upper Yangtze Block of South China during Lower Cambrian, and sampling location (modified from Ren et al. (2016); Liu et al. (2017); Zhang et al. (2019); Liu et al. (2022)). **(b)** Stratigraphic histogram of Qiongzhusi Formation in the well WY1H in Weiyuan area. CLP: Canglangpu Formation.

in the well W-A. However, the Lower Cambrian shale gas has not been commercially developed in this area, and the uncertainty of gas-bearing properties greatly limits the further exploration in this area (Wang et al., 2019a; Rao et al., 2022; Li et al., 2022a).

3. Samples and experiments

3.1. Samples

Eight black shale samples were collected from the Lower Cambrian Qiongzhusi Formation at the well WY1H in the Weiyuan area, Sichuan Basin (Fig. 1). The well is structurally located at the Leshan-Weiyuan slope of Mianyang-Changning craton rift. The regional sedimentary background shows that the Qiongzhusi Formation in the Weiyuan area deposited in the deep-water shelf environment (Fig. 1(a)). The Qiongzhusi Formation black shale at this well has a cumulative thickness of 80 m, with a burial depth of 4393.62–4451.37 m (Fig. 1(b)), and it is deemed to be a potential shale gas reservoir (Ren et al., 2016, 2017).

3.2. Experiments

3.2.1. Organic geochemical analysis

TOC content was measured by the LECO CS-230 carbon and sulfur analyzer (Liu et al., 2013). The sample was crushed into powder (<200 mesh, about 100 mg), treated with 5% dilute hydrochloric acid to remove carbonate minerals, then rinsed with deionized water to neutral and dried for 4 h. TOC content was quantified by CO_2 peak area produced by OM combustion (Table 1).

The maturity of shale samples was obtained by laser Raman method (Beyssac et al., 2002; Quirico et al., 2005; Henry et al., 2019). The used instrument was a HORIBA-JY Lab RAM automatic micro-Raman spectroscopy. The measured OM was solid bitumen. The Raman spectra were fitted by the bimodal method as proposed by Wang et al. (2015). The parameter of RBS (the distance between G and D bands) was used to calculate EqRo with the equation: $EqRo = 0.0537 \times RBS - 11.21$ (Liu et al., 2013). Five different solid bitumen particles were measured for each sample and their EqRo values were averaged. It should be pointed out that although the equation of Liu et al. (2013) is based on vitrinite, they also measured the Raman spectra of different macerals (such as solid bitumen, amorphous organic matter, and vitrinite-like maceral) in over-mature shale, and found that there were no significant differences in their Raman parameters. Therefore, this equation can be also applicable to solid bitumen in over-mature shale, as used in literatures (e.g., Wang et al., 2021; Li et al., 2023a; Xiang et al., 2024).

The mineral composition of shale samples was analyzed by XRD. The instrument used was a Rigaku MiniFlex-600 diffractometer. The main analytical conditions included a voltage of 40 kV, a current of 15 mA, a scanning range of $2\theta = 3°–80°$, a slit width of 1 mm, and a scanning speed of 1°/min. The results were analyzed using the Lorentz polarization software to obtain semi-quantitative data on the mineral composition (Pecharesky and Zavalij, 2005).

3.2.2. Extraction and elemental analysis of kerogen

Kerogen was isolated from shale samples by chemical methods (Suleimenova et al., 2014). The main procedures were as follows: (1) the sample was crushed to less than 100 mesh; (2) carbonate was eliminated by HCL acid; (3) silicate was removed by HF acid; (4) pyrite was removed by $CrCl_2$ solution; (5) the obtained sample was washed with deionized water and dried to obtain kerogen.

The contents of nitrogen (N), carbon (C), hydrogen (H) and sulfur (S) in isolated kerogen samples were analyzed using the Elementar Vario EL-III. The results were corrected with BBOT ($C_{26}H_{26}N_2O_2S$) standard sample. Each sample was measured three times, and the relative error was required to be less than 5%, and the average values were taken (Gai et al., 2020).

3.2.3. Low-pressure gas adsorption experiments

According to the International Union of Pure and Applied Chemistry (IUPAC), shale nanopores were divided into micropores (<2 nm), mesopores (2–50 nm), and macropores (>50 nm) (Chalmers et al., 2009). In this study, the sum of mesopores and

Table 1
Analysis data of TOC contents, EqRo values and mineral compositions of bulk shale samples.

Sample	Depth, m	TOC, %	EqRo, %	Mineral composition, %							
				Q	Fel	Car	Py	I/S	Ill	K	Chl
1	4393.62	1.55	3.45	40.93	15.81	4.67	2.22	5.61	17.28	3.79	9.70
2	4395.65	1.31	3.49	38.90	15.35	5.24	3.41	3.89	18.91	2.34	11.97
3	4413.70	2.42	3.46	39.36	21.54	1.46	3.58	8.29	14.20	3.18	7.49
4	4417.74	1.79	nd	33.97	25.40	3.47	2.73	1.96	21.88	2.74	7.85
5	4433.40	3.39	3.49	48.26	19.71	1.53	3.13	3.39	17.74	1.01	5.23
6	4435.50	4.09	3.48	46.69	17.14	4.21	2.98	5.11	13.72	2.45	6.02
7	4437.46	4.12	3.49	49.11	17.48	7.51	2.97	2.83	12.06	0.76	7.28
8	4451.37	0.59	nd	34.38	18.01	2.03	3.51	14.03	21.33	0.99	5.73

Notes: Q, Fel, Car, Py, I/S, Ill, K and Chl are Quartz, Feldspar, Carbonate, Pyrite, mixed I/S, Illite, kaolinite, and Chlorite, respectively. nd means not data. The data of sample 5 is from Xing et al. (2025).

macropores were defined as non-micropores. The shale and isolated kerogen samples were analyzed by a Micromeritics ASAP 2020 analyzer, and LPNA (N_2 adsorption) and LPCA (CO_2 adsorption) experiments were conducted to characterize their non-micropores and micropores, respectively. About 1 g of shale samples and about 0.15 g of kerogen samples (20–40 mesh) were used. They were dried for 12 h in an oven at 110 °C to remove their moisture and volatile components before the adsorption experiments. The relative pressure of LPNA experiments was from 0.005 to 0.995, with a temperature of 77.35 K, while for the LPCA experiments, the relative pressure was from 0.0001 to 0.032 and the temperature was 273.15 K.

Based on the LPNA adsorption data, the non-micropore specific surface area (S_{non}) was calculated using the modified Brunauer-Emmett-Teller (BET) equation (Tian et al., 2015), and the pore size distribution (PSD) of non-micropores was calculated using the Barrett-Joyner-Halenda (BJH) model (Barrett et al., 2014). According to the LPCA data, the micropores volume (V_{mic}) was obtained by the Dubinin-Astakhov (D-A) equation (Dubinin, 1989; Sing et al., 2012).

Zhang et al. (2020) conducted research on pore structure of bulk shale and its isolated kerogen, and indicated that it was feasible to use kerogen to investigate pore structure of OM in bulk shale. Li et al. (2023b) further roughly calculated the pore structure parameters of inorganic minerals (IM) according to the pore structure parameters of the bulk shale and isolated kerogen. According to their method, the specific surface area and pore volume of OM and IM pores in shale can be calculated by Eqs. (1), (3) and (4), respectively:

$$S_{OM} = \frac{S_{kerogen}}{TOC_{kerogen}} \times TOC_{shale} \tag{1}$$

$$S_{IM} = S_{shale} - S_{OM} \tag{2}$$

$$V_{OM} = \frac{V_{kerogen}}{TOC_{kerogen}} \times TOC_{shale} \tag{3}$$

$$V_{IM} = V_{shale} - V_{OM} \tag{4}$$

where S_{shale}, S_{IM} and $S_{kerogen}$ represent the specific surface areas of shale, inorganic minerals, and kerogen, respectively; V_{shale}, V_{IM} and $V_{kerogen}$ represent the pore volumes of shale, inorganic minerals, and kerogen, respectively; TOC_{shale} and $TOC_{kerogen}$ represent the TOC content of the shale and kerogen, respectively (the carbon content of kerogen is equivalent to its TOC content).

3.2.4. Water vapor adsorption experiments

The particle size of a sample will have a certain influence on its adsorption (Li et al., 2020; Dang et al., 2021), therefore, the WVA experiment used the same sample size (20–40 mesh) as the low-pressure gas adsorption experiment. The instrument used was a Quantachrome Aquadyne DVS WVA analyzer, and it has the advantages of high automation, accurate control of relative humidity (RH), high repetition of experimental results (a relative error of less than 3%) (Yang et al., 2021). About 100 mg of shale sample and 10 mg of kerogen sample were used, and they were dried at 100 °C for 48 h to remove water before adsorption experiments. The experimental temperature was 298.5 K, and the RH was from 2% to 95%. The specific experimental steps were strictly followed as reported by Sang et al. (2019). In order to ensure the reliability of experimental data, the experiment was repeated for three times for each sample, and their average was taken.

In the present study, Dent model was applied to fit the WVA data of shale and kerogen samples, as suggested by Dang et al. (2021). Compared with other models, this model has a higher fitting degree to the test data, and can calculate the primary and secondary adsorption amounts which are conducive to discuss the adsorption kinetics process (Dent, 1977; Tang et al., 2017; Duan and Li, 2018; Wang et al., 2019b; Yang et al., 2020a). According to the Dent multilayer adsorption model, the WVA capacity, primary adsorption capacity and secondary adsorption capacity of shale and kerogen samples can be described by the following equations, respectively:

$$q = \frac{q_{mD} k_{D1}\left(\frac{P}{P_0}\right)}{\left(1 - k_{D2}\left(\frac{P}{P_0}\right)\right)\left(1 + k_{D1}\left(\frac{P}{P_0}\right) - k_{D2}\left(\frac{P}{P_0}\right)\right)} \tag{5}$$

$$q_1 = \frac{q_{mD} K_{D1}\frac{P}{P_0}}{1 - K_{D2}\frac{P}{P_0} + K_{D1}\frac{P}{P_0}} \tag{6}$$

$$q_2 = \frac{q_{mD} K_{D1} K_{D2}\left(\frac{P}{P_0}\right)^2}{\left(1 - K_{D2}\frac{P}{P_0}\right)\left(1 - K_{D2}\frac{P}{P_0} + K_{D1}\frac{P}{P_0}\right)} \tag{7}$$

where q is the adsorption capacity of sample; P is the equilibrium vapor pressure; P_0 is the saturated vapor pressure at the experimental temperature; P/P_0 is the relative pressure which is equivalent to the RH of water vapor; q_1 and q_2 represent the adsorption capacity (mg/g) of primary and secondary sites, respectively; q_{mD} is Dent monolayer capacity; and k_{D1} and k_{D2} are adsorption constants related to the primary adsorption energy and secondary adsorption energy, respectively.

In the MATLAB software, the initial values of q_{mD}, k_{D1} and k_{D2} need continuously to be adjusted to achieve relatively suitable fitting results according to the following principles, i.e., q_{mD} must not be negative, k_{D1} is generally much larger than k_{D2}, and k_{D2} is generally less than 1.

The pore size distribution from WVA data obtained by Kelvin equation can be compared with that of low-pressure N_2 adsorption (Zolfaghari et al., 2017b). Therefore, in the present study, Kelvin equation was used to characterize the pore size distribution of water vapor adsorption for both the shale and kerogen samples. The calculation method is as follows:

$$\ln\left(\frac{1}{\mathrm{RH}}\right) = \frac{2\gamma V_m \cos\theta / TR}{r_p} \tag{8}$$

where RH represents relative humidity; γ is the surface tension of water at the experimental temperature, 0.07038 N/m; V_m is the molar volume of water vapor, 1.8×10^{-5} m^3/mol; θ is the contact angle between water and porous solid, and it was calculated according to $\theta = 0°$; T is the experimental temperature, 298.15 K; R is the universal gas constant, 8.314 J $mol^{-1}K^{-1}$; r_p is the pore diameter, and this parameter was calculated at the maximum RH of 95% (Xiong et al., 2023).

Since the pore size does not depend on the molecules of the above equation (Yang et al., 2020a), it was calculated by Eq. (9), representing the filling of capillary condensate in a certain width pore under a certain RH condition (Zolfaghari et al., 2017b):

$$r_p = -\frac{RT\left[\ln\left(\frac{1}{\mathrm{RH}}\right)\right]^2}{2\gamma V_m \cos\theta} \times \frac{d\Phi_w}{d\ln\left(\frac{1}{\mathrm{RH}}\right)} \tag{9}$$

where Φ_w is the pore volume fraction, with a value $\leq r_p$, which does not represent the actual pore diameter. Before the capillary condensation, water vapor can be adsorbed on the pore surface through multilayer adsorption with a specific thickness, so the thickness (t) formed by multilayer adsorption needs to be considered when calculating the pore diameter. The actual pore diameter (d) can be calculated by Eq. (10):

$$d = 2(r_p + t) \tag{10}$$

The thickness of adsorption layer t in Eq. (10) is obtained by Halsey equation:

$$t = 0.354\left[-5\left(\ln\left(\frac{P}{P_0}\right)\right]^2 \tag{11}$$

3.2.5. Hysteresis characteristic description

There is usually a hysteresis of desorption compared with adsorption for the low-pressure gas or water vapor adsorption-desorption isotherms of organic-rich shale samples, which results in a hysteresis loop (Sing et al., 1985; Tang et al., 2017; Yang et al., 2020a). The shape and area of hysteresis loop can effectively reflect the pore structure and retention effect on adsorbed gas (Thommes et al., 2015; Xu et al., 2020; Song et al., 2023). The hysteresis loop can be quantitatively characterized by the Area hysteresis Index (AHI) (Tang et al., 2017; Ukaomah et al., 2023). This study used Eq. (12) recommended by Tang et al. (2017) to calculate the hysteresis index of low-pressure gas and water vapor isotherms for the shale and kerogen samples:

$$\mathrm{AHI} = \frac{A_{de} - A_{ad}}{A_{de}} \times 100 \tag{12}$$

where A_{de} and A_{ad} represent the area under the desorption and adsorption isotherms, respectively.

4. Results

4.1. Shale TOC content, maturity, mineral composition, and kerogen elemental composition

The shale samples have a TOC content of 0.59%–4.12%, with an average of 2.41%, and the EqRo value of 3.45%–3.49%, with an average of 3.48% (Table 1), indicating that they are rich in OM, and in the over-mature stage. It is worth noting that the second-order Raman peak appears at 2688.52 cm^{-1} (Fig. 2), indicating that the OM has been graphitized (Kelemen and Fang, 2001).

The main minerals of shale samples are clay minerals and quartz minerals. The content of total clay minerals ranges from 22.93% to 42.08%, with an average of 32.59%. Among the clay minerals, illite is dominant, ranging from 12.06% to 21.88%, with an average of 17.14%. Other clay minerals include chlorite, kaolinite and illite-montmorillonite mixed layer, with contents of 5.23%–11.97%, 0.76%–3.79% and 1.96%–14.03%, respectively, with average values of 7.66%, 2.16% and 5.64% respectively (Table 1). The quartz, content ranges from 33.97% to 49.11%, with an average of 41.45%. Feldspar and carbonate have a content of 15.35%–25.40% and 1.46%–7.51%, respectively, with an average of 18.81% and 3.77%, respectively. In addition, the shale has a small amount of pyrite, with a content range of 2.22%–3.51% (Table 1).

For the shale samples, there is a positive correlation between the TOC and quartz contents ($R^2 = 0.7904$, Fig. 3(a)), which means that the quartz may be primarily derived from biogenesis (Gareth et al., 2012; Marin-Carbonne et al., 2014; Tatzel et al., 2017). The TOC content is negatively correlated with clay minerals ($R^2 = 0.9504$, Fig. 3(b)), which is attributed to the decrease of total clay content with the increase of quartz content. These results are similar to those reported previously for the other Lower Cambrian over-mature shale samples from the Sichuan Basin and its surrounding areas (Tian et al., 2013, 2015; Cheng et al., 2017; Xu et al., 2022).

The elemental composition of kerogen samples is shown in Table 2. The contents of N, C, H and S elements are 0.82%–1.25%, 72.94%–85.57%, 2.03%–2.48% and 1.25%–9.18%, respectively. It should be pointed out that kerogen is not pure OM, and a well-

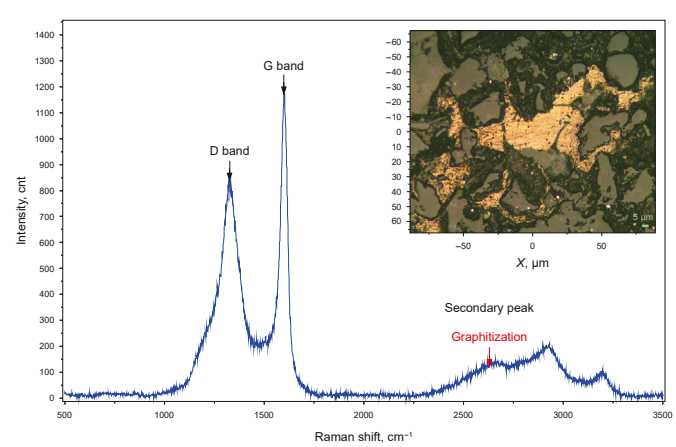

Fig. 2. Laser Raman spectrum of solid bitumen from Sample 7.

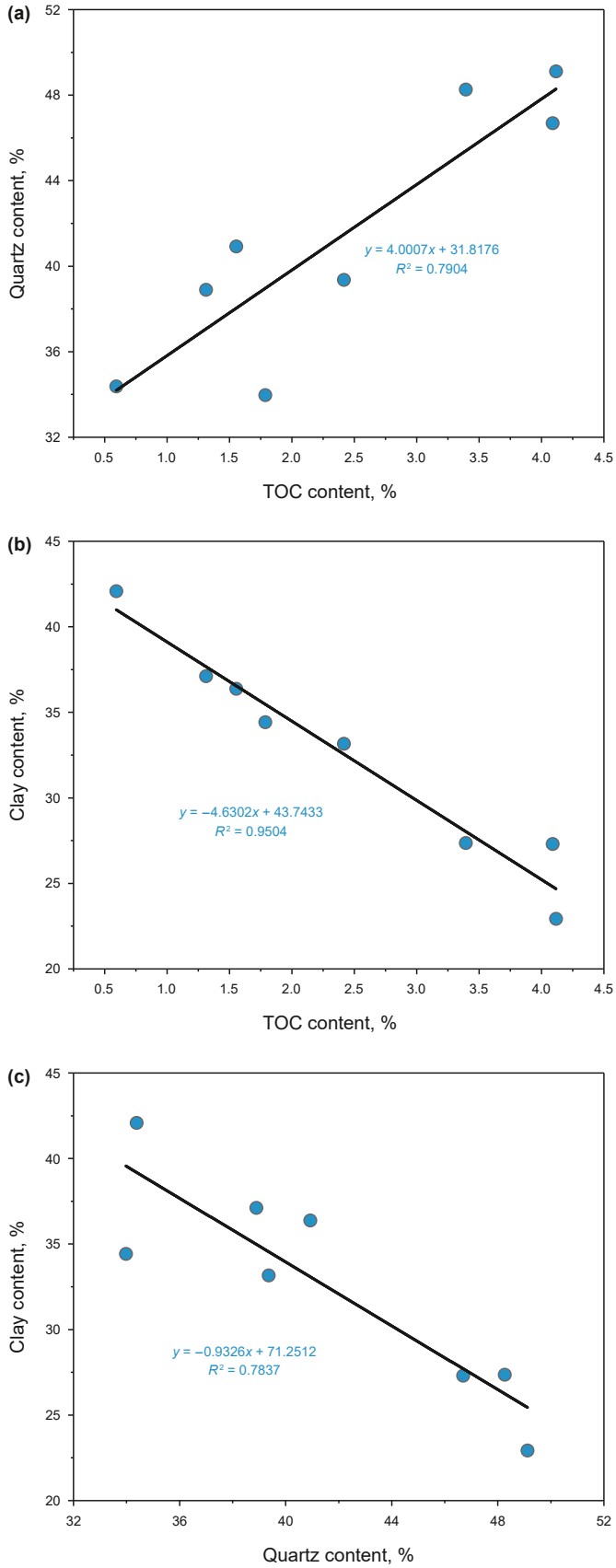

Fig. 3. The relationships of TOC with quartz **(a)** and clay minerals **(b)**, and the correlation between quartz and clay minerals **(c)** for shale samples.

Table 2
Element contents of isolated kerogen from bulk shale samples.

Sample	Element content of kerogen, %			
	N	C	H	S
1	0.82	77.73	2.31	1.38
2	0.82	76.94	2.22	1.27
3	0.99	81.79	2.28	1.40
4	0.94	80.15	2.25	1.25
5	1.25	85.57	2.23	1.36
6	0.93	72.94	2.03	9.18
7	1.00	83.94	2.36	1.75
8	0.70	78.75	2.48	1.71

isolated kerogen sample should have a carbon content of more than 70% (Suleimenova et al., 2014; Hou et al., 2020), thus the kerogen samples in the present study are all well-isolated. Sample 6 has a high S content, which may be related to the incomplete removal of pyrite. Since the inorganic carbon was completely removed in the process of kerogen isolation, the carbon content of kerogen samples can be used as their TOC content.

4.2. Low pressure gas adsorption isotherms and pore structure parameters

4.2.1. Adsorption isotherm characteristics

Fig. 4(a)–(b) shows the N_2 adsorption-desorption isotherm of the shale samples. According to the classification of IUPAC (Thommes et al., 2015), their adsorption isotherm and hysteresis patterns are divided into Type IV and Type H3, respectively, which indicates that there are capillary condensation and evaporation processes, and mainly contains mesopores with a slit shape (Sing et al., 1985; Cao et al., 2015). The N_2 adsorption and desorption isotherms of kerogen samples are shown in Fig. 4(c)–(d). Their adsorption isotherm type is also type IV, but the hysteresis loop is basically disappeared. This means that the hysteresis loop of the shale samples is mainly caused by their inorganic nanopores, but has little relationship with their OM nanopores. This is quite similar with the results from Lu et al. (2023). The CO_2 adsorption isotherms of the shale and kerogen samples are shown in Fig. 5. Both of them are type I isotherm (Thommes et al., 2015). When $P/P_0 = 0.997$, the N_2 adsorption capacities of the shale and kerogen samples are 2.29–8.38 cm^3/g and 239.66–355.23 cm^3/g, respectively. When $P/P_0 = 0.03$, the CO_2 adsorption capacities of the shale and kerogen samples are 0.82–1.86 cm^3/g and 15.25–23.96 cm^3/g, respectively. The N_2 and CO_2 adsorption capacities of kerogen samples are much higher than those of shale samples, indicating that the shale OM has more nanopores than minerals, including non-micropores and micropores.

4.2.2. Pore structure parameters

Table 3 shows the pore structure parameters of the shale and kerogen samples, in which the pore structure parameters of OM and minerals in the shale samples were calculated by Eqs. (1)–(4). For the shale samples, the non-micropore surface area (S_{non}) and micropore volume (V_{mic}) have a range of 1.74–11.97 m^2/g (an average of 7.93 m^2/g) and 0.00245–0.006746 cm^3/g (an average of 0.004983 cm^3/g), respectively. For the kerogen samples, the S_{non} and V_{mic} have a range of 179.95–243.36 m^2/g (an average of 213.13 m^2/g) and 0.07202–0.09586 cm^3/g (an average of 0.08872 cm^3/g), respectively. In the shale samples, the OM S_{non} and V_{mic} have a range of 1.36–11.06 m^2/g, (an average of 6.42 m^2/g) and 0.000543–0.005073 cm^3/g (an average of 0.002742 cm^3/g), respectively, and the inorganic S_{non} and V_{mic} have a range of 0.38–2.31 m^2/g (an average of 1.50 m^2/g) and 0.001112–0.00313 cm^3/g (an average

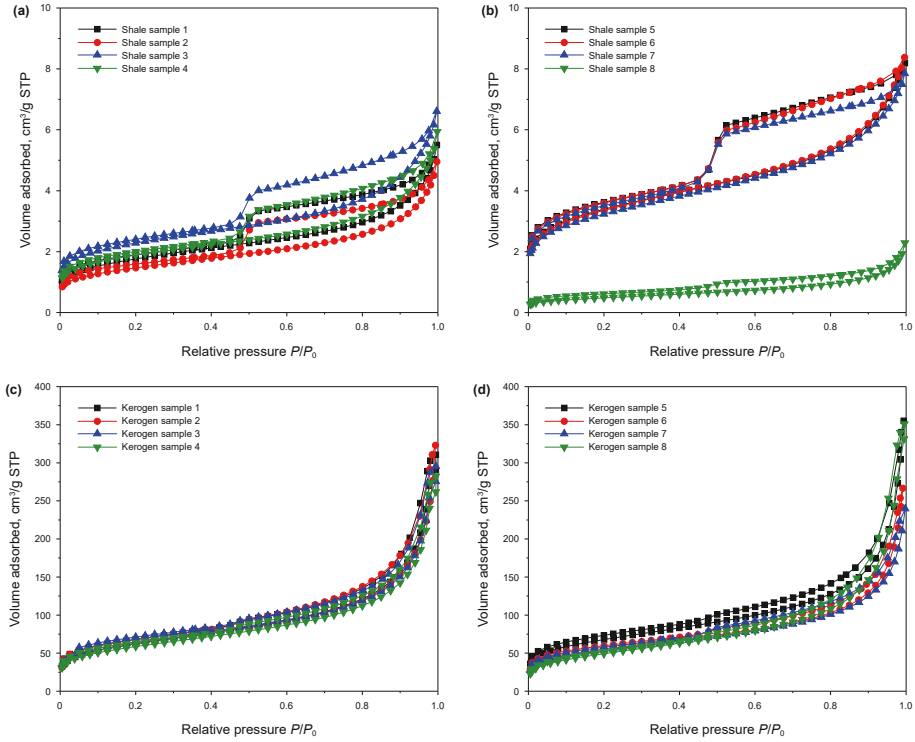

Fig. 4. N_2 adsorption-desorption isotherms of shale ((**a**)–(**b**)) and kerogen ((**c**)–(**d**)) samples.

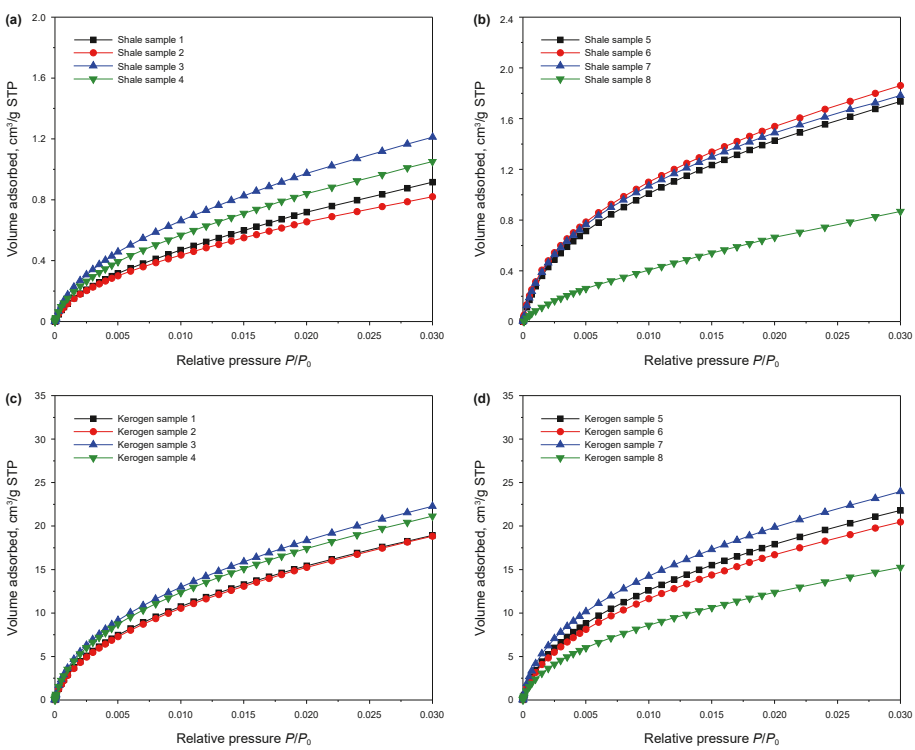

Fig. 5. CO_2 adsorption isotherms of shale ((**a**)–(**b**)) and kerogen ((**c**)–(**d**)) samples.

of 0.002241 cm^3/g), respectively. The relationships between the TOC content of shale samples and the pore structure parameters of their OM and IM nanopores clearly indicate that the OM S_{non} is greater than the IM S_{non} for the all samples (Fig. 6(a)), while the OM V_{mic} is greater than the IM V_{mic} (Fig. 6(b)) for the samples with TOC >2.09%.

4.3. Water vapor adsorption characteristics and parameters

4.3.1. Adsorption isotherm characteristics

The water vapor adsorption-desorption isotherms of shale and kerogen samples are shown in Fig. 7(a) and (b). According to the

Table 3
The pore structure parameters of bulk shale, kerogen and shale OM and IM.

Sample	S_{non}, m^2/g				V_{mic}, cm^3/g			
	Bulk shale	Kerogen	OM	IM	Bulk shale	Kerogen	OM	IM
1	6.31	224.65	4.49	1.82	0.004888	0.08797	0.001758	0.003130
2	5.25	224.08	3.82	1.43	0.004502	0.08855	0.001510	0.002992
3	8.08	232.57	6.87	1.20	0.004931	0.09586	0.002833	0.002098
4	6.70	210.68	4.70	2.01	0.005054	0.08982	0.002003	0.003051
5	11.97	243.36	9.65	2.31	0.005606	0.09173	0.003638	0.001968
6	11.91	197.34	11.06	0.84	0.006746	0.09048	0.005073	0.001673
7	11.46	192.41	9.44	2.02	0.005687	0.09329	0.004575	0.001112
8	1.74	179.95	1.36	0.38	0.002450	0.07202	0.000543	0.001907

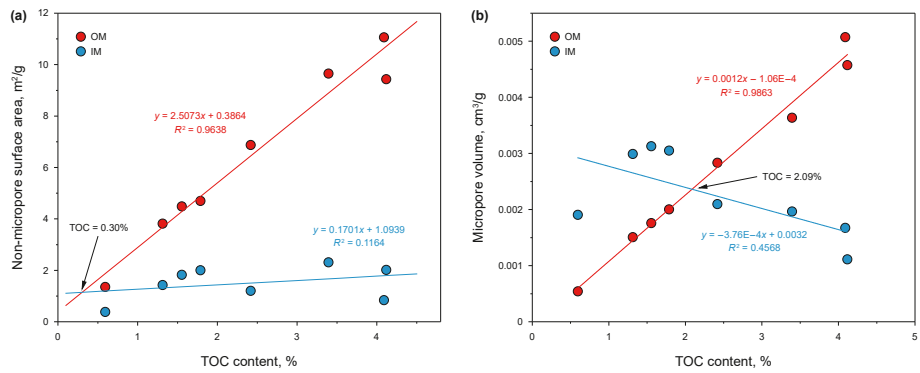

Fig. 6. Correlation of TOC content of shale samples with the S_{non} **(a)** and V_{mic} **(b)** of their OM and IM.

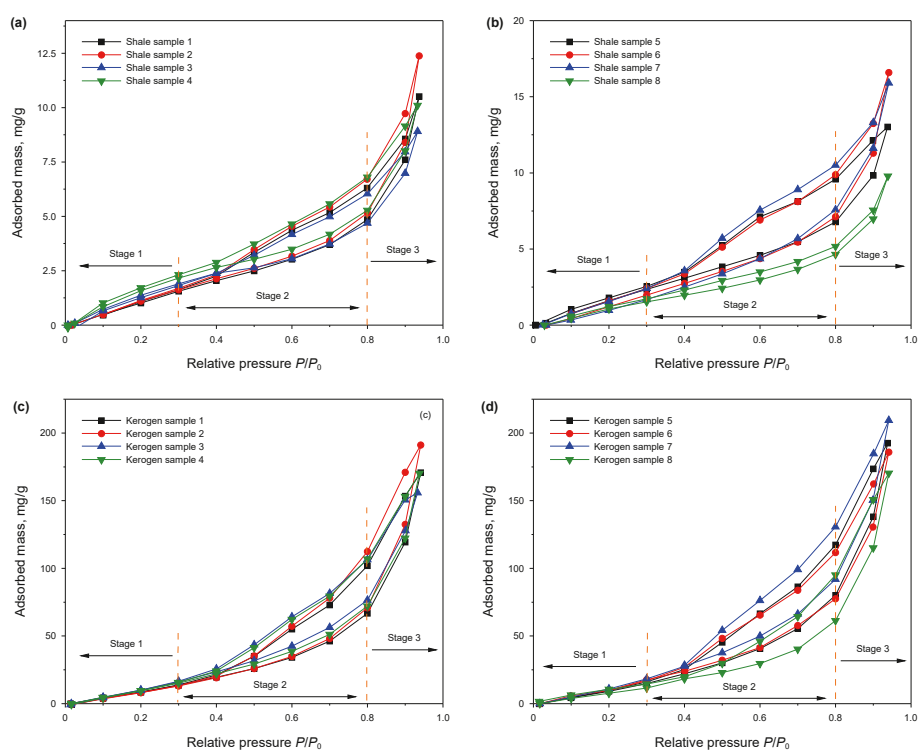

Fig. 7. The water vapor adsorption isotherms of shale (**(a)**–**(b)**) and kerogen (**(c)**–**(d)**) samples (T = 298.15 K).

classification of the IUPAC (Sing et al., 1985), the isotherms of all samples belong to the Type II. These isotherms can be roughly divided into three stages (Fig. 7): a predominant monolayer adsorption as RH < 0.3, a main multilayer adsorption as RH between 0.3 and 0.8, and a predominant capillary condensation as RH > 0.8 (Wan et al., 2016; Tang et al., 2017). It should be noted that due to the differences in the composition and pore structure of different samples, the RH values corresponding to the turning

points of adsorption curves will be slightly different, but the characteristics of three stages are similar. All shale and kerogen samples exhibit a significant desorption hysteresis at the higher RH range, with the type H_3 hysteresis loop based on the IUPAC classification (Fig. 7). Table 4 shows the nitrogen adsorption and WVA AHI values of the shale and kerogen samples calculated according to Eq. (12). The AHIN (nitrogen hysteresis index) of the shale samples ranges from 18.21% to 27.74%, with an average of 21.28%, and that of kerogen samples ranges from 8.59% to 13.12%, with an average of 10.91%. The AHIW (water vapor hysteresis index) of the shale samples ranges from 3.28% to 41.31%, with an average of 20.74%, and that of kerogen samples ranges from 28.6% to 37.4%, with an average of 33.62%.

4.3.2. Primary and secondary adsorption

The Dent adsorption model was used to fit the WVA data of the shale and kerogen samples (RH = 0.2–0.95), resulting in a perfect fit (Fig. 8), with average R^2: values of 0.9930 for the shale samples and 0.9996 for kerogen samples, and the three fitting parameters (K_{D1}, K_{D2} and q_{mD}) are presented in Table 5. The K_{D1} and K_{D2} of the shale samples range from 3.39 to 12.12 (mean 8.66) and 0.88 to 0.95 (mean 0.91), respectively, and the K_{D1} and K_{D2} of the kerogen samples range from 2.53 to 3.82 (mean 3.11) and 0.92 to 0.97 (mean 0.95), respectively. It is clear that the strength and binding energy of the primary adsorption are much higher than those of the secondary adsorption for the two kinds of samples. The q_{mD} of shale samples range from 1.3 to 2.29 mg/g (mean 1.7 mg/g), and that of kerogen samples range from 14.96 to 25.82 mg/g (mean 20.08 mg/g).

According to the fitting parameters of the Dent adsorption model, the WVA capacities of shale and kerogen samples at RH = 0.95 were further calculated by Eqs. (5)–(7) (Table 6). For the kerogen samples, the q, q_1 and q_2 have a range of 155.81–209.30 mg/g (mean 181.79 mg/g), 14.55–24.76 mg/g (mean 19.33 mg/g) and 153.91–182.84 mg/g (mean 160.71 mg/g), respectively. For the shale samples, the q, q_1 and q_2 have a range of 8.91–16.59 mg/g (mean 12.15 mg/g), 1.28–2.19 mg/g (mean 1.66 mg/g), and 7.14–14.33 mg/g (mean 160.71 mg/g), respectively. According to these data, the secondary adsorption capacities of kerogen and shale samples are significantly higher than their primary adsorption capacities. This phenomenon confirms that higher adsorption intensity does not mean higher adsorption capacity. Comparing the q_1 at RH = 0.95 with the monolayer water content q_{mD} fitted by the Dent model, it was found that the former is slightly smaller than the latter, which indicates that some adsorption sites in the shale or kerogen samples are still not occupied by water molecules even under a very high *RH* condition (Švábová et al., 2011).

Table 4
AHI values of bulk shale and kerogen samples.

Sample	Area hysteresis index (AHI), %			
	Bulk shale		Kerogen	
	AHIN	AHIW	AHIN	AHIW
1	20.31	23.22	11.07	34.63
2	22.65	23.15	12.65	36.77
3	18.21	3.28	8.59	28.60
4	22.50	9.34	11.11	34.11
5	20.46	19.45	10.15	35.76
6	19.34	33.17	9.55	31.33
7	19.03	41.31	13.12	30.35
8	27.74	13.04	11.00	37.40

Note: AHIN means AHI value of low pressure N_2 adsorption curve; AHIW means AHI value of WVA curve.

It can be seen from the relationship between the RH and the primary and secondary adsorption capacities of water vapor in Fig. 8 that the variation trends of the shale and kerogen samples are similar. With increasing RH, their primary adsorption and the secondary adsorption capacities gradually increase. In the low RH region (<0.1), the primary adsorption capacity increases sharply with the increase of RH, without few secondary adsorptions, and the adsorption mainly occurs at the high binding energy positions due to the direct contact of water vapor with the surface of nanopores (Duan and Li, 2018; Li et al., 2021a; Liang et al., 2023). When the RH increases to about 0.5, the q_1 and q_2 are equal. With the further increase of RH, the q_1 basically remains unchanged since the high binding energy sites are gradually occupied, while the q_2 increases rapidly in an exponential function trend. It is worth noting that the primary adsorption has the characteristics of type I isotherm (Fig. 8), with a strong adsorption effect (Xie et al., 2023), while the secondary adsorption has the characteristics of type III isotherm (Fig. 8), with a weak adsorption effect (Donohue and Aranovich, 1998; Czepirski et al., 2000). This indicates that in the whole adsorption behavoir, the primary adsorption is the monolayer adsorption, and the secondary adsorption includes the multilayer adsorption and capillary condensation. Generally speaking, water vapor tends to be adsorbed at the primary adsorption sites with higher binding energy, while the secondary adsorption amount is much greater than the primary adsorption amount due to the greater storage of water in multilayer adsorption and capillary condensation effect. This also explains the periodic characteristic of the water vapor isotherm on mechanism (Fig. 7).

5. Discussion

5.1. Comparison of pore structure from nitrogen and water vapor adsorption

5.1.1. Hysteresis characteristics

Comparing Fig. 4 with Fig. 7, it can be seen that the hysteresis loops of N_2 and water vapor adsorption-desorption of the samples (the shale and kerogen) are different. This is related to the different properties of the two kinds of probe molecules. The hysteresis loop of N_2 is mainly controlled by the chemical properties of pores and their geometry which is related to the open cylindrical, ink bottle, parallel plate and slit-like pores (Sing et al., 1985; Sing and Williams, 2004; Xu and Prodanovic', 2018). In the process of WVA, a larger hysteresis loop area indicate that water molecules have stronger interaction with pore wall and more water persists in pore spaces (Yang et al., 2020a; Liang et al., 2023). This phenomenon is considered to be closely related to the oxygen-containing functional groups on the surface of pore wall, the van der Waals force and the capillary condensation effect in ink bottle-shaped pores (Gregg et al., 1967; McCutcheon and Barton, 1999) or swelling caused by water retention between clay mineral layers (Charrière and Behra, 2010). In addition, the AHIN value of kerogen is significantly lower than that of the shale (Table 4). The AHIN value of the shale is negatively correlated with its TOC content, but positively correlated with the clay mineral content (Fig. 10(a)–(b)). Therefore, it can be believed that the pores of minerals (mainly clay minerals) mainly control the area of hysteresis loop of nitrogen adsorption-desorption curve in the shale.

Different from the nitrogen adsorption-desorption curve hysteresis characteristics, the AHIW value of kerogen samples is much greater than that of shale samples, which is consistent with the research results of Ukaomah et al. (2023) on marine and lacustrine shale and kerogen. The largest difference in the AHIW value between the shale and kerogen samples occurs at about RH = 0.8, where the kerogen is an order of magnitude greater than the shale

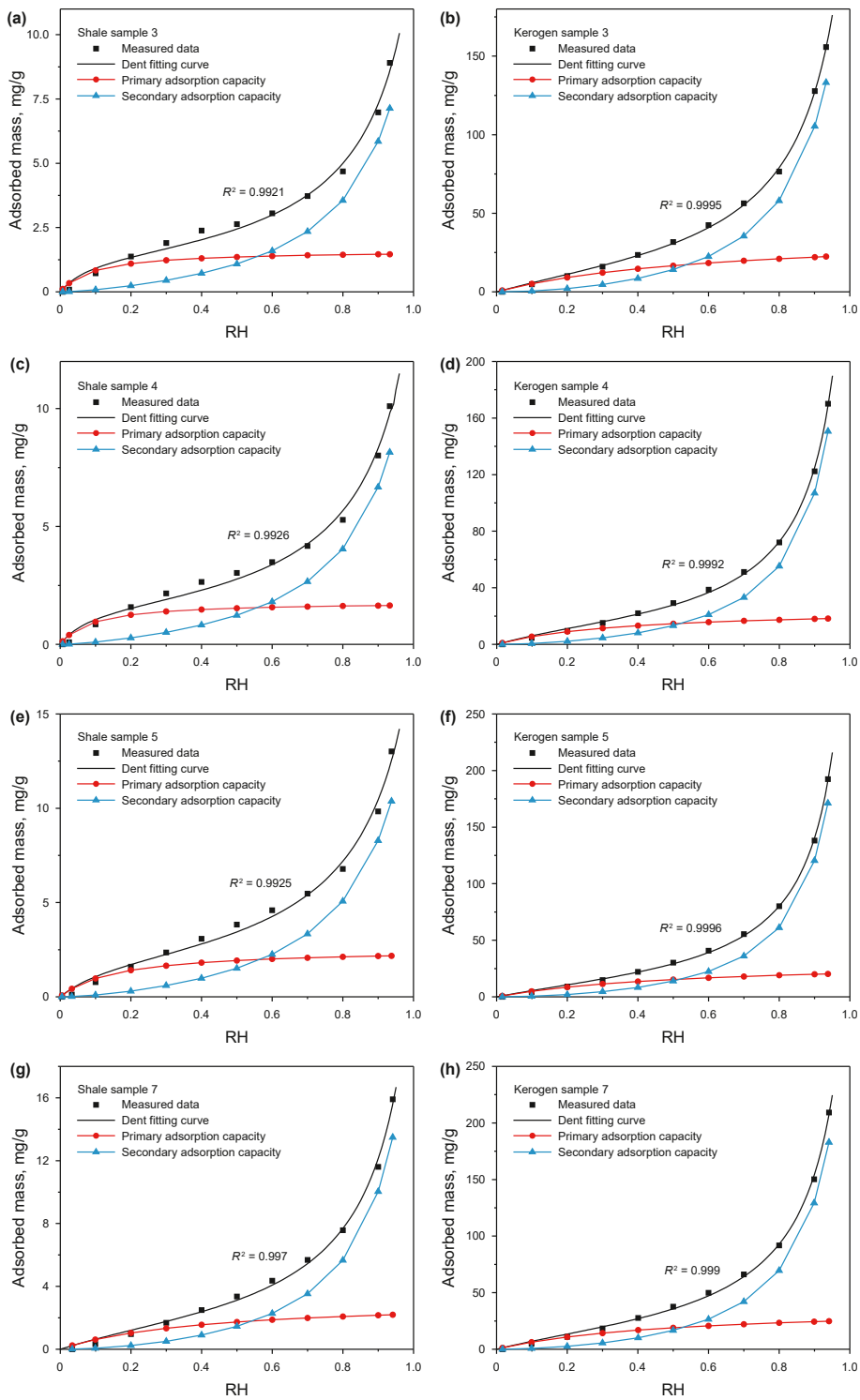

Fig. 8. Water vapor adsorption isotherms of selected shale and kerogen samples.

(Fig. 9). In addition, the AHIW value of the shale is significantly positively correlated with the TOC content, but has not correlation with the clay mineral content (Fig. 10(c)–(d)). The greater AHIW value of kerogen samples and the positive correlation between the TOC content and AHIW value of shale samples together indicate a positive role of over-mature OM in the hydrophilicity of the shale.

5.1.2. Pore size distribution characteristics

When the porous medium has pores that can be penetrated by water vapor, the WVA curve can be characterized according to the Kelvin equation (Eqs. (9)–(11)) (Hagymassy et al., 1969; Hagymassy and Brunauer, 1970). Fig. 11 shows the pore size distribution (PSD) of shale and kerogen samples obtained by WVA and N_2 adsorption.

Table 5
The physical parameters of water vapor adsorption of bulk shale and kerogen samples.

Sample	Parameters							
	Bulk shale				Kerogen			
	q_{mD}, mg/g	K_{D1}	K_{D2}	R^2	q_{mD}, mg/g	K_{D1}	K_{D2}	R^2
1	1.34	9.02	0.93	0.9945	17.12	3.31	0.96	0.9998
2	1.30	11.47	0.95	0.9932	18.42	2.54	0.96	0.9999
3	1.49	11.67	0.89	0.9921	23.80	2.53	0.92	0.9995
4	1.67	12.12	0.89	0.9926	18.78	3.71	0.95	0.9992
5	2.23	7.02	0.88	0.9925	21.08	2.77	0.95	0.9996
6	1.92	6.61	0.94	0.9936	20.66	3.82	0.95	0.9999
7	2.29	3.39	0.91	0.9970	25.82	2.96	0.94	0.9990
8	1.35	7.95	0.92	0.9920	14.96	3.27	0.97	0.9998

Table 6
Water vapor capacity of bulk shale and kerogen samples.

Sample	WVA capacity, mg/g					
	Bulk shale			Kerogen		
	q	q_1	q_2	q	q_1	q_2
1	10.51	1.32	8.93	170.75	16.61	153.91
2	12.38	1.28	10.77	191.08	17.74	173.55
3	8.91	1.46	7.14	155.81	22.43	133.22
4	10.10	1.65	8.15	170.15	18.21	150.62
5	13.02	2.17	10.37	192.47	20.26	171.12
6	16.59	1.88	14.33	185.89	20.05	164.49
7	15.90	2.19	13.48	209.30	24.76	182.84
8	9.79	1.32	8.14	178.89	14.55	155.96

For WVA, the PSD of shale and kerogen samples is unimodal, with the peak at 2–3 nm and about 3.5 nm, respectively, but their PSD from nitrogen adsorption, has not an obvious peak, presenting a decrease with the increase of pore sizes. In the pore size range of 1–100 nm, the PSD value obtained by WVA is greater than that obtained by N_2 adsorption for the shale samples, especially in the pore size range of 2–5 nm (Fig. 11(a)), while the PSD curves obtained by the two methods basically coincides for the kerogen samples (Fig. 11(b)). Since the PSD from WVA indicates the distribution of hydrophilic pores (Zolfaghari et al., 2017b), it can be further believed, combined with the results of this study, that hydrophilicity exists in the nanopores with different pore sizes of the over-mature kerogen. and water vapor is mainly adsorbed on the surface of small non-microporous pores(2–5 nm)in the shale. In addition, the results (Fig. 11) also indicate that, due to the influence of minerals, there are a large number of pores in the shale samples where water molecules can enter but nitrogen molecules cannot (such as interlayer pores of clay minerals) (Yang et al., 2020a, 2020b; Gao et al., 2022). Therefore, combining the adsorption process of water vapor and and nitrogen, it is quite useful to understand not only their PSD of shale samples, but also the hydophilicity of shale OM and mineral pores.

5.2. Effect of shale composition on water vapor adsorption

It is generally believed that the oxygen-containing functional groups in shale clay minerals and OM are the main primary adsorption sites (Bai et al., 2020), and water vapor can be adsorbed by molecular layer and capillary condensation with a high binding energy (Duan and Li, 2018; Sang et al., 2019), while the hydrophobic organic pores and the sites upon the primary adsorption are the main secondary adsorption sites (Wang et al., 2020a; Chen et al., 2021b). Fig. 12(a) shows the positive relationships of TOC content with the WVA capacities of q, q_1 and q_2 at RH = 0.95 for the shale samples, with R^2 of 0.6456, 0.7778 and 0.5628, respectively, which implicate that the OM in the over-mature shale is still an important carrier in the process of primary and secondary adsorption of water vapor at high RH. In addition, the correlation between TOC content and q_1 is better than that between TOC content and q and q_2 (Fig. 12(a)), and the monolayer adsorption of water vapor in the shale is positively correlated with TOC content (Fig. 12(b)). These indicate that even in the over-mature stage of Lower Cambrian shale in this study, the hydrophilic oxygen-containing functional groups may still remain, so that with a significant monolayer water vapor adsorption on the surface of OM pores (Xie et al., 2023). The study from Bai et al. (2020) implicates that the primary adsorption capacity will gradually increase with the decrease of pore sizes. Therefore, the primary adsorption capacity of OM with abundant micropores will increase with the increase of TOC contents. Previous studies have suggested that hydrophobic OM has little contribution to the water vapor primary adsorption of shale (Sondergeld et al., 2010; Odusina et al., 2011), but for the present study shale, the strong correlation between the TOC content and the primary adsorption capacity indicates the importance of OM on the primary adsorption of shale, which may be neglected previously, at least for over-mature shale.

Inorganic minerals (mainly clay minerals) in shale are generally hydrophilic (Boyer et al., 2006; Borysenko et al., 2009), and pore water mainly distributes in their pores (Passey et al., 2010; Sondergeld et al., 2010; Korb et al., 2014; Li et al., 2016). However, the WVA capacity of the shale in this study is negatively correlated with the clay minerals content (Fig. 13), which does not mean that the clay minerals have no contribution to the WVA. Considering the obvious negative correlation between the TOC and clay mineral

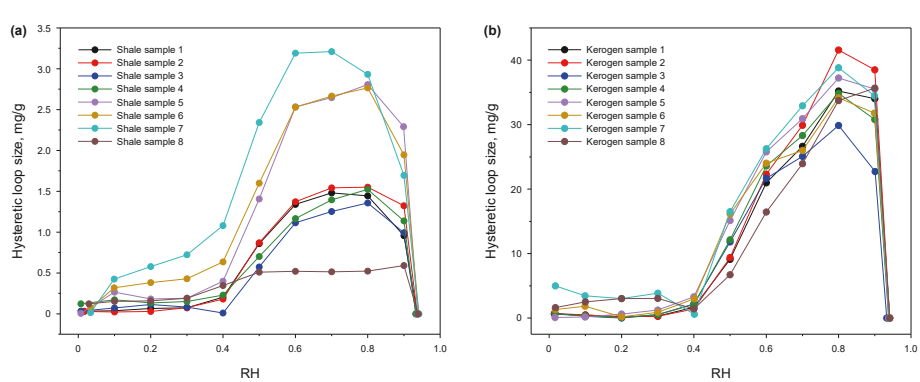

Fig. 9. Variations in hysteresis loop sizes of shale **(a)** and kerogen **(b)** samples at different RH values. Hysteresis loop size is the difference of adsorption amount between desorption and adsorption curves.

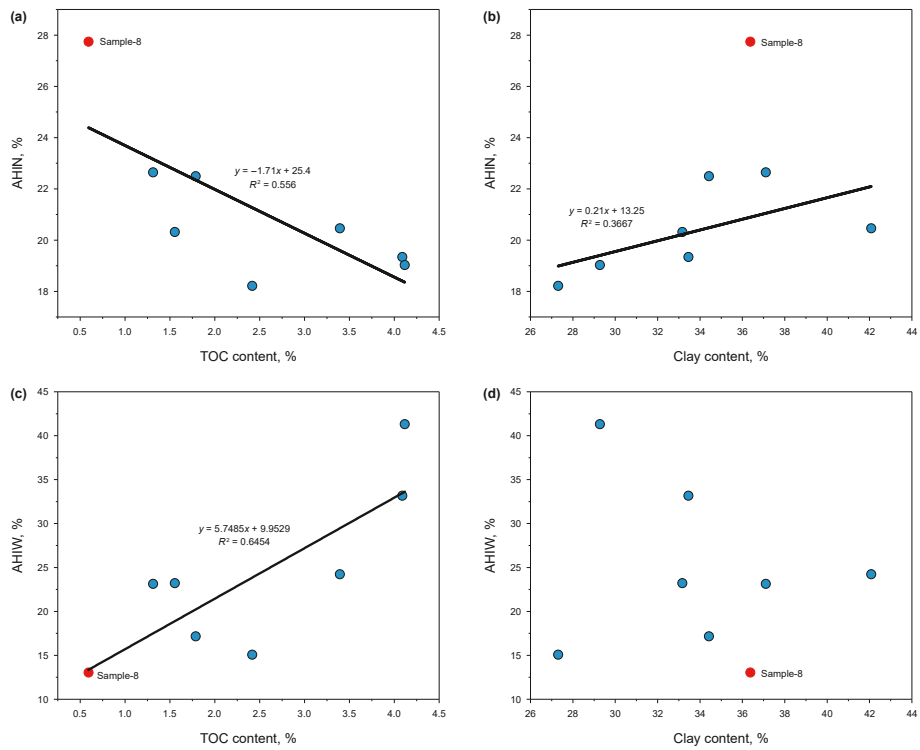

Fig. 10. Relationships of AHI value with TOC content and clay mineral content of shale samples. **(a)** and **(b)**: N_2 adsorption; **(c)** and **(d)**: Water vapor adsorption.

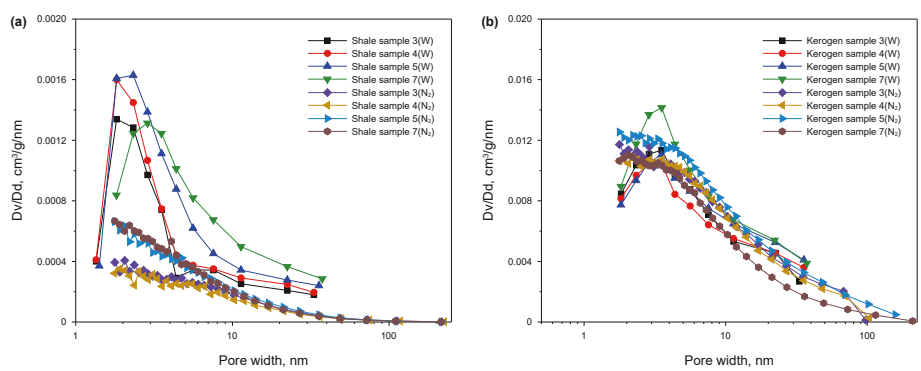

Fig. 11. Comparison of PSD from nitrogen and water vapor adsorption for representative shale **(a)** and kerogen **(b)** samples, W and N_2 represent water vapor and nitrogen adsorption, respectively.

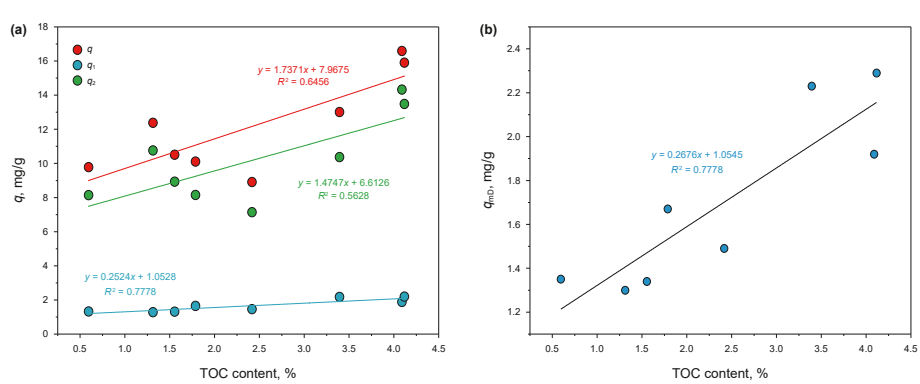

Fig. 12. **(a)** Correlations between water vapor adsorption capacity and TOC content for shale samples (T = 298.15 K); **(b)** Correlation between monolayer adsorption capacity and TOC content for shale samples.

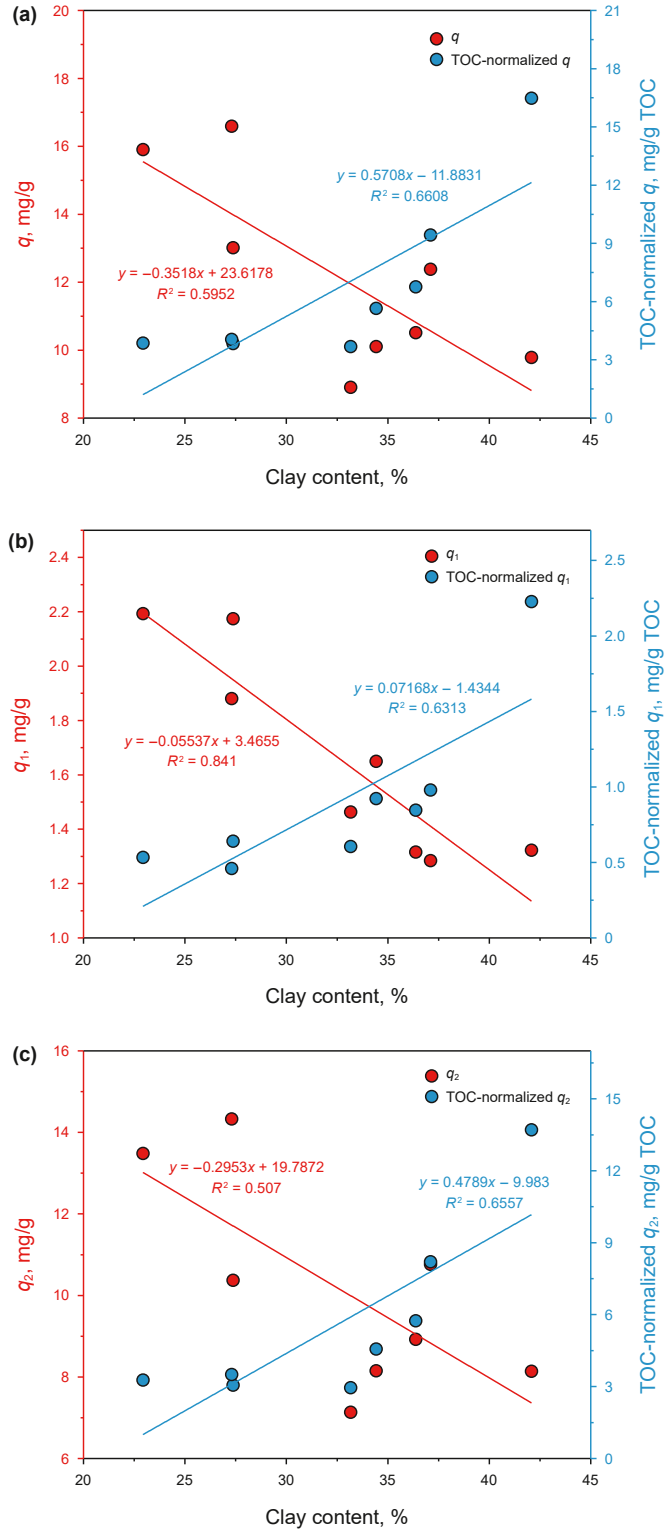

Fig. 13. **(a)** Relationships of clay mineral content with water vapor adsorption capacity, **(b)** primary adsorption capacity, and **(c)** secondary adsorption capacity for shale samples before and after TOC normalization.

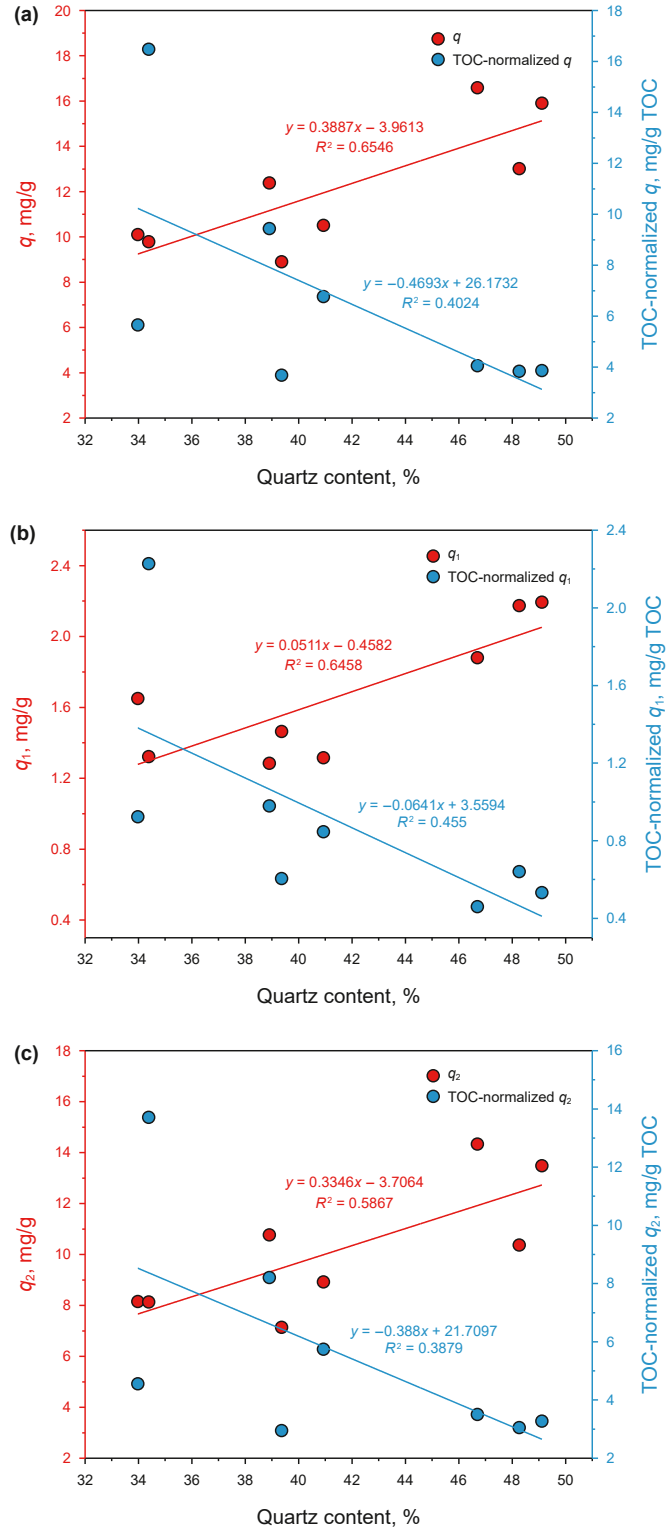

Fig. 14. **(a)** Relationships of quartz content with water vapor adsorption capacity, **(b)** primary adsorption capacity, and **(c)** secondary adsorption capacity for shale samples before and after TOC normalization.

contents in the shale (Fig. 3(b)), this study further analyzed the correlation between the clay minerals and the TOC-normalized WVA capacity. The results show that the clay mineral content is positively correlated with the TOC-normalized WVA capacity (Fig. 13), indicating that the clay minerals also have a positive effect on the water vapor adsorption. Similarly, considering the obvious positive correlation between the TOC and quartz contents (Fig. 3(a)), the relationships between the quartz content and the

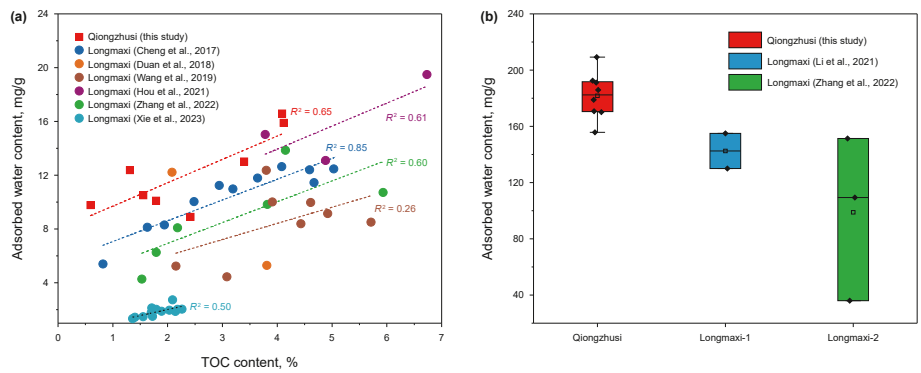

Fig. 15. Comparison of water adsorption ability between the Lower Cambrian Formation and Lower Silurian Longmaxi Formation samples. **(a)** Comparison of shale samples. The EqRo of Longmaxi Formation shale samples range from 1.93% to 3.12%. The data comes from Cheng et al. (2017); Duan and Li (2018); Wang et al. (2019b); Hou et al. (2021); Zhang et al. (2022c) and Xie et al. (2023). **(b)** Comparison of kerogen samples. The EqRo of Longmaxi Formation samples range from 2.24% to 2.95%. The data comes from Li et al. (2021b) and Zhang et al. (2022a).

WVA capacities before and after TOC normalization were separately investigated. As the results presented in Fig. 14, the quartz content has a positively correlation with the WVA capacity before the TOC normalization, but has a negative correlation with the WVA capacity after the TOC normalization, indicating that the contribution of quartz to the water vapor adsorption of shale is negative, which is similar to the Longmaxi Formation shale (Ge et al., 2020; Hou et al., 2021; Cheng et al., 2022).

In order to further clarify the water adsorption property of Lower Cambrian shale and kerogen in this study, the data of Longmaxi Formation shale and kerogen (EqRo between 1.93% and 3.12%) reported in literatures were compared and analyzed. As shown in Fig. 15, the water adsorption capacity of the samples (shale and kerogen) in this study is significantly greater than that of the Longmaxi Formation samples (shale and kerogen). This further indicates that the strong water adsorption capacity of the shale in this study should be related to the strong water adsorption capacity of its OM.

With the increase of thermal maturation, the oxygen-containing functional groups of OM in shale are gradually fall off, with a decrease of the hydrophilicity (Hu et al., 2015, 2016). At the same time, the OM will evolve into a stable and orederly chemical structure, and finally transform into a layered graphite-like structure (Huang et al., 2018; Hou et al., 2019). When R_o arrives to 3.4–3.5%, there is a jump on the chemical structure of OM, with the transformation from amorphous carbon to crystalline graphite, i.e., the extent of graphitization is significantly enhanced (Wang et al., 2018, Wang and Li, 2018; Hou et al., 2019). In this study, the EqRo of Lower Cambrian shale is between 3.45% and 3.49%, which is just at this "jump point" of maturity, and the OM has been significantly graphitized as presented in Fig. 2, while the maturity of the Longmaxi Formation samples in Fig. 15 is significantly lower than this point, and the OM has not been significantly graphitized. Previous studies shown that the basal plane of graphitic carbon is hydrophilic in nature (Kozbial et al., 2014; Liubov et al., 2018; Zhang et al., 2022b), and the high hydrophilicity of graphite may originate from the charge transfer between graphite and water molecules through H-π interaction, with an average water contact angle of less than 30° (Zhang et al., 2022b). Therefore, the graphitization of OM in shale will lead to the enhancement of its hydrophilicity, and the very high maturity of the Lower Cambrian shale in the present study should be the basic reason for the strong water adsorption ability of its OM.

Table 7
Water vapor adsorption capacity of shale organic and inorganic nanopores.

Sample	WVA capacity, mg/g						A1	B1
	Organic nanopores			Inorganic nanopores				
	q_{OM}	$q_{1\text{-}OM}$	$q_{2\text{-}OM}$	q_{IM}	$q_{1\text{-}IM}$	$q_{2\text{-}IM}$		
1	3.41	0.33	3.08	7.10	0.98	5.85	32.45	67.55
2	3.26	0.30	2.96	9.12	0.98	7.81	26.33	73.67
3	4.61	0.66	3.94	4.30	0.80	3.20	51.71	48.29
4	3.79	0.41	3.36	6.31	1.24	4.79	37.54	62.46
5	7.63	0.80	6.79	5.38	1.37	3.59	58.64	41.36
6	10.42	1.12	9.22	6.17	0.76	5.11	62.81	37.19
7	10.26	1.21	8.97	5.64	0.98	4.52	64.55	35.45
8	1.35	0.11	1.18	8.44	1.21	6.96	13.78	86.22

Note: A1 is the ratio of WVA capacity of organic nanopores to that of bulk shale (%), B1 is the ratio of WVA capacity in inorganic nanopores to that of bulk shale. The WVA capacity of bulk shale is from Table 4.

5.3. Water vapor adsorption capacity of organic and inorganic pores

As mentioned aforehand, water vapor can be adsorbed into the organic and inorganic pores in the shale. According to the WVA capacities of the shale and kerogen, the WVA capacity in organic and inorganic pores of the shale can be quantitatively evaluated using the following calculation formula:

$$q_{OM} = \frac{q_{kerogen}}{TOC_{kerogen}} \times TOC_{kerogen} \tag{13}$$

$$q_{IM} = q_{shale} - q_{OM} \tag{14}$$

where q_{OM}, $q_{kerogen}$, q_{IM} and q_{shale} are the WVA capacities of organic matter, kerogen, inorganic matter and shale, respectively.

Using the same method as described above, the primary and secondary adsorption capacity of kerogen can be converted into the primary and secondary adsorption capacity of OM, i.e., $q_{1\text{-}OM}$ and $q_{2\text{-}OM}$, respectively, and then the $q_{1\text{-}OM}$ and $q_{2\text{-}OM}$ can be used to further obtain the primary and secondary adsorption of minerals, i.e., $q_{1\text{-}IM}$ and $q_{2\text{-}IM}$, respectively. It should be noted that the external surface adsorption of kerogen is not considered in these calculations, and the obtained WVA capacity of organic pores may be greater than that in shale, but it can still provide a reference for clarifying the WVA behavior of the organic and inorganic pores in shale. The calculated results are all presented in Table 7.

Considering the obvious positive correlation between the TOC content and WVA capacity of the shale (Fig. 12), the influence of TOC contents on the WVA capacity in its OM and IM pores was

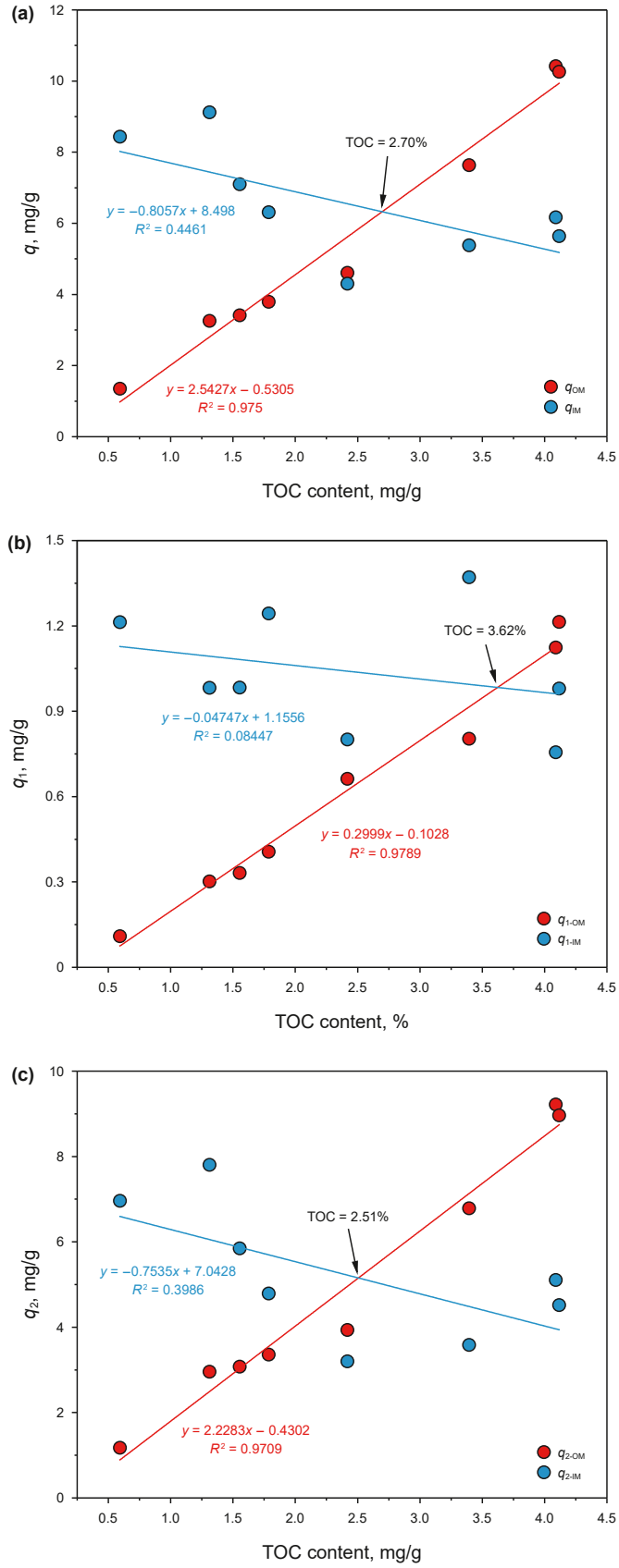

Fig. 16. **(a)** Correlations of TOC content with the WVA capacity, **(b)** primary adsorption capacity and **(c)** secondary adsorption capacity of the organic and inorganic pores in shale samples.

further discussed by applying the calculation results in Table 7. With the increase of TOC contents, the q_{OM} of the shale increases significantly, while the q_{IM} gradually decreases (Fig. 16(a)). When the TOC content is more than 2.70%, the q_{OM} is larger than the q_{IM}, indicating that the water-holding capacity of organic pores in the shale is slightly greater than that of inorganic pores at higher TOC contents. For more details, with the increase of TOC contents, the $q_{1\text{-OM}}$ and $q_{2\text{-OM}}$ increases significantly, while the $q_{1\text{-IM}}$ remains basically unchanged and the $q_{2\text{-IM}}$ gradually decreases (Fig. 16(b), (c)). When the TOC content is larger than 2.51%, the $q_{2\text{-OM}}$ is greater than the $q_{2\text{-IM}}$, and when the TOC content is larger than 3.62%, the $q_{1\text{-OM}}$ is greater than the $q_{1\text{-IM}}$ (Fig. 16(b), (c)). These indicate that water vapor may be preferentially adsorbed on oxygen-containing groups or graphite-like structures on the surface of organic pores under the condition of a higher TOC content, and the clustered water mass and capillary condensate will also preferentially gather in the OM pores. Comparing with the TOC content corresponding to the above three turning points in Fig. 16, the turning point of primary adsorption has a higher TOC content, which should be related to the strong hydrophilicity and more hydrophilic sites of the inorganic mineral itself. As pointed out above, the calculated WVA value of organic pores is higher. Thus, the TOC content at the turning point should be actually much greater.

According to the data in Tables 6 and 7, the distribution of adsorbed water in the organic and inorganic pores was calculated. An average of 44.39% of the adsorbed water is stored in the organic pores of shale, of which the primary and secondary adsorption account for 4.98% and 39.41%, respectively. An average of 55.61% of the adsorbed water is stored in the inorganic pores of shale, of which 9.29% is primary adsorption and 46.32% is secondary adsorption. Therefore, for the studied shale, the WVA capacity in the inorganic pores is averagely greater than that in the organic pores. This should be related to its higher clay and lower TOC contents (Table 1).

5.4. Effect of pore structure on water vapor capacity

The adsorbed water in shale occurs as a condensed state in micropores, which is mainly controlled by the micropore volume (V_{mic}), while it exists as an adsorbed phase in non-micropores, which is mainly controlled by the non-micropores specific surface area (S_{non}) (Borysenko et al., 2009; Charrière and Behra, 2010; Zolfaghari et al., 2017b; Chen et al., 2021a; Sun et al., 2021; Xu et al., 2022). Therefore, the effects of V_{mic} and S_{non} on WVA was investigated for the studied shale.

Fig. 17(a) and (b) show that there are good positive correlations between the shale pore structure parameters (V_{mic} and S_{non}) and its total WVA capacity (q), primary adsorption capacity (q_1) and secondary adsorption capacity (q_2), which indicates that both the micropores and non-micropores play an important role in the water vapor adsorption behavior. Comparatively speaking, the S_{non} of shale plays a major role in the primary adsorption since the R^2 value of S_{non} vs. q_1 ($R^2 = 0.7542$) is significantly larger than that of V_{mic} vs. q_1 ($R^2 = 0.4344$), while the secondary adsorption of the shale is affected by the combination effect of V_{mic} and S_{non} based on their similar R^2 values with q_2 (Fig. 17(a)–(b)). This shows that the non-micropores of shale provide adsorption sites available for water vapor monolayer adsorption as well as spaces for the multilayer adsorption structures of water molecules significantly to increase the water adsorption capacity. Both of the OM V_{mic} and S_{non} have significant positive correlations with the shale q, q_1 and q_2 (Fig. 17(c)–(d)), while the IM V_{mic} and S_{non} have weak negative correlations or no clear relationship with the shale q, q_1 and q_2, respectively (Fig. 17(e)–(f)), which further indicate that the organic pores in shale play a major role in its WVA.

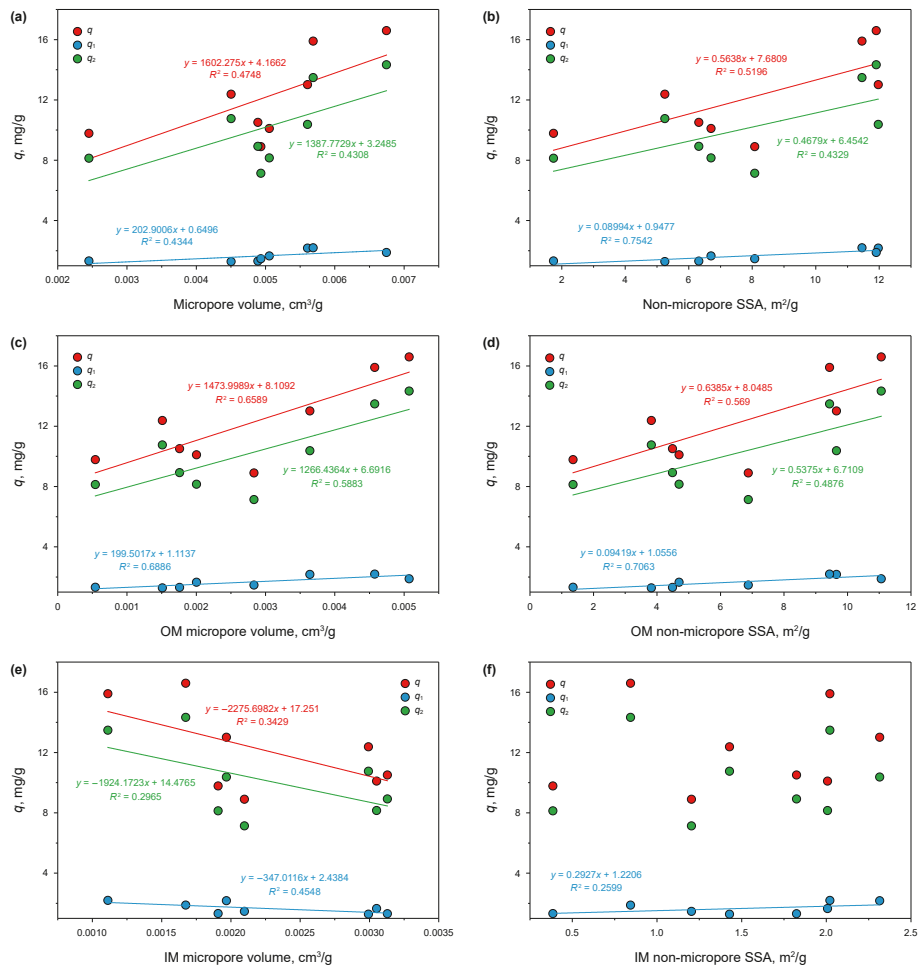

Fig. 17. Correlations between the pore structure parameters (V_{mic} and S_{non}) of shale ((**a**)–(**b**)), shale OM ((**c**)–(**d**)) and shale inorganic mineral ((**e**)–(**f**)) and the water vapor adsorption capacity (q, q_1 and q_2) of shale (RH = 0.95, T = 298.15 K).

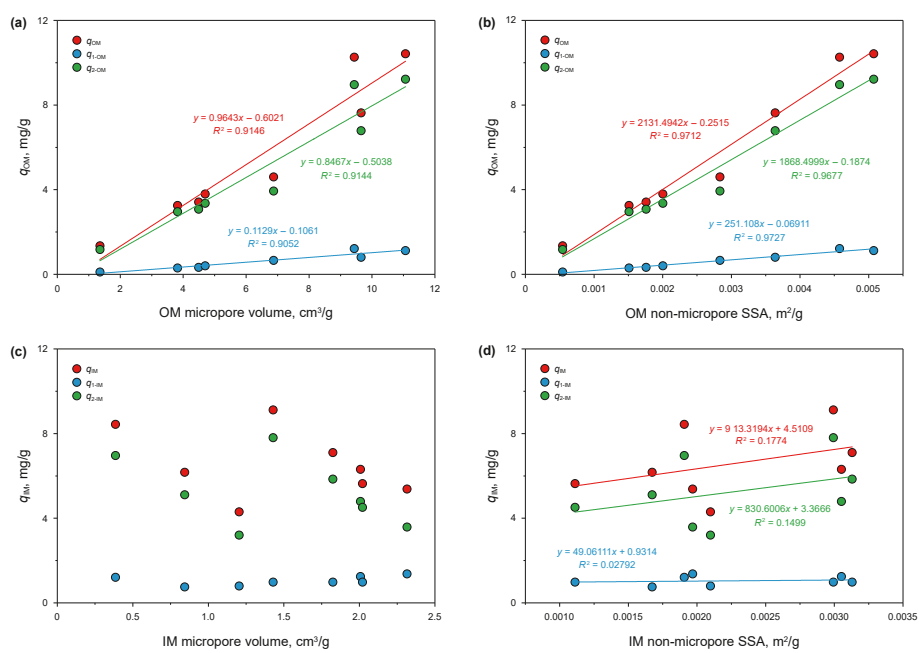

Fig. 18. Correlation between pore structure parameters (V_{mic} and S_{non}) of organic ((**a**)–(**b**)) and inorganic ((**c**)–(**d**)) pores and their water vapor adsorption capacity (RH = 0.95, T = 298.15 K).

The adsorption behavior of water vapor in the organic and inorganic pores of shale was further discussed by applying the data in Tables 3 and 7 The results show that the OM V_{mic} and S_{non} are strongly positively correlated with its WVA capacity (q_{OM}, $q_{1\text{-}OM}$ and $q_{2\text{-}OM}$) (Fig. 18(a)–(b)), indicating that the micropores and non-micropores all have an important contribution to the WVA behavior of OM, and both of them have primary and secondary adsorption. There is no correlation between the V_{mic} of IM and its WVA capacity (Fig. 18(c)), while the S_{non} of IM shows a weak positive correlation with its WVA (Fig. 18(d)), indicating that the non-micropores of inorganic minerals (especially clay minerals) make a major contribution to its WVA, including primary and secondary adsorption, which should be attributed to the fact that the clay minerals mainly develop non-micropores (Yang et al., 2018).

5.5. Geological implications

In the Sichuan Basin and its surrounding areas, the gas in-place (GIP) content of Lower Cambrian shale is commonly lower than that of the Longmaxi Formation shale. Apart from the poor preservation conditions of the Lower Cambrian, which lead to continuous leakage and diffusion of natural gas, its inherently higher maturity is also a significant factor (Wang et al., 2014, 2020b; Zhao et al., 2016; Dong et al., 2016). Excessively high maturity (EqRo>3.0%–3.5%) will lead to the decrease of shale porosity and the change of shale pore structure, thus reducing the reservoir physical property of shale (Curtis et al., 2012; Chen and Xiao, 2014; Zou et al., 2015; Xiao et al., 2015). In this study, through the WVA study of Lower Cambrian over-mature shale from the Weiyuan area, Sichuan Basin, and the comparison of its results with the data of Longmaxi Formation shale reported in literatures, it was found that the shale has stronger water adsorption capability, which may be another important factor affecting the GIP content.

Quite a few studies show that the main EqRo range of Longmaxi shale in the Sichuan Basin and its surrounding area is between 2.0% and 3.0% (Nie et al., 2009; Wang et al., 2009, 2013b; Xiao et al., 2015), without reaching the critical point of OM carbonization (3.4%–3.5% EqRo), and the water adsorption of its OM is relatively low (Sun et al., 2021). In contrast, the Lower Cambrian shale has a higher maturity, with an EqRo value of 3.0%–4.5% in most areas (Yan et al., 2016; Zhao et al., 2019; Li et al., 2022a). For the present study shale, the average EqRo is 3.48%, and the OM has already been graphitized, with obvious hydrophilicity. It can be predicted that the Lower Cambrian shale in the other areas of Sichuan Basin with an EqRo>3.5% will have stronger graphite extent and hydrophilicity, which is disadvantageous to shale gas storage.

On the other hand, according to the present study results, the OM of Lower Cambrian shale has a stronger water adsorption capability than the minerals, and the shale water adsorption capacity increases with increasing TOC content. This further implicates that under poor preservation conditions, a high TOC content does not mean a high adsorbed gas content or GIP content for the Lower Cambrian shale with a very high maturity. The exploration of Lower Cambrian shale gas in Southern China also proves this point. Here is an example. The TOC content of Lower Cambrian shale in the Changning area of Sichuan Basin is between 2.0% and 5.94%, with an average of 3.2%, and the EqRo is as high as 3.5%–4.2%, with an average of 4.0%, The shale reservoir contains only a minor amount of gas, with a GIP content of 0.0–0.8 m^3/t (an average 0.65 m^3/t), but has a high-water saturation (Zhao et al., 2016). Therefore, for the evaluation and exploration of over-mature shale gas, it is necessary to fully consider the OM graphitization extent and water adsorption performance, as well as the occurrence and distribution characteristics of adsorbed water in shale nanopores, which would be an important factor affecting the GIP content.

6. Conclusion

Based on the study on the WVA characteristics, influencing factors and mechanisms of Lower Cambrian over-mature shale and its kerogen from the Weiyuan area, Sichuan Basin, the main conclusions are as follows.

(1) The WVA isotherms of shale and kerogen are type II, and there are obvious hysteresis loops in the multilayer adsorption range. The kerogen has greater WVA capacity and hysteresis index than the shale, indicating that the shale OM is relatively hydrophilic
(2) The shale OM has much stronger WVA capacity than the clay minerals, leading to the TOC content has a main control on the WVA capacity of shale. The extremely high maturity of the shale (an average EqRo of 3.48%) with a significant graphitization of OM is the main reason for its strong hydrophilicity.
(3) The micropores and non-micropores of shale all play an important role in WVA behavior. There are primary and secondary adsorption in the OM micropores and non-micropores, while the WVA in inorganic minerals is mainly related to their non-micropores.
(4) For the Lower Cambrian shale reservoirs in southern China, the TOC content and maturity jointly control the hydrophilicity, and then affect the GIP content, which should be highly addressed in the shale gas exploration and development.

CRediT authorship contribution statement

Yi-Jie Xing: Writing – original draft, Validation, Methodology, Investigation, Data curation. **Xian-Ming Xiao:** Writing – review & editing, Supervision, Resources, Funding acquisition. **Peng Cheng:** Resources. **Yan-Ming Zhao:** Conceptualization. **Wei Liu:** Conceptualization.

Declaration of competing interest

The authors declare that they have no known competing financial interests or personal relationships that could have appeared to influence the work reported in this paper.

Acknowledgments

This study was supported by the National Natural Science Foundation of China (42030804; 42330811) and the “Deep-time Digital Earth” Science and Technology Leading Talents Team Funds for the Central Universities for the Frontiers Science Center for Deep-time Digital Earth, China University of Geosciences (Fundamental Research Funds for the Central Universities; grant number: 2652023001).

References

Arthur, E., Tuller, M., Moldrup, P., de Jonge, L.W., 2016. Evaluation of theoretical and empirical water vapor sorption isotherm models for soils. Water Resour. Res. 52, 190–205. https://doi.org/10.1002/2015WR017681.
Bai, J.J., Kang, Y.L., Chen, M.J., et al., 2020. Impact of surface chemistry and pore structure on WVA behavior in gas shale. Chem. Eng. J. 402, 126238. https://doi.org/10.1016/j.cej.2020.126238.
Barrett, E.P., Joyner, L.G., Halenda, P.P., 2014. The determination of pore volume and area distributions in porous substances. I. Computations from nitrogen isotherms. J. Am. Chem. Soc. 73 (1), 373–380. https://doi.org/10.1021/ja01145a126.
Beyssac, O., Goffé, B., Chopin, C., et al., 2002. Raman spectra of carbonaceous material in metasediments: a new geothermometer. J. Metamorph. Geol. 20 (9), 859–871. https://doi.org/10.1046/j.1525-1314.2002.00408.x.
Borysenko, A., Clennell, B., Sedev, R., et al., 2009. Experimental investigations of the

wettability of clays and shales. J. Geophys. 114 (7), B07202. https://doi.org/10.1029/2008JB005928.
Boyer, C., Kieschnick, J., Suarez-Rivera, R., et al., 2006. Producing gas from its source. Oilfield Rev. 18 (3), 36–49.
Cao, T.T., Song, Z.G., Wang, S.B., et al., 2015. A comparative study of the specific surface area and pore structure of different shales and their kerogens. Sci. China Earth Sci. 58 (4), 510–522. https://doi.org/10.1007/s11430-014-5021-2.
Chalmers, G., Bustin, R.M., Powers, I., 2009. A Pore by Any Other Name Would Be as Small: the Importance of Meso- and Microporosity in Shale Gas Capacity. AAPG Annual Convention and Exhibition, Denver, Colorado.
Charrière, D., Behra, P., 2010. Water sorption on coals. J. Colloid Interface Sci. 344 (2), 460–467. https://doi.org/10.1016/j.jcis.2009.11.064.
Chen, J., Xiao, X.M., 2014. Evolution of nanoporosity in organic-rich shales during thermal maturation. Fuel 129, 173–181. https://doi.org/10.1016/j.fuel.2014.03.058.
Chen, J., Gai, H.F., Xiao, Q.L., 2021a. Effects of composition and temperature on water sorption in over-mature Wufeng-Longmaxi shales. Int. J. Coal Geol. 234, 103673. https://doi.org/10.1016/j.coal.2020.103673.
Chen, J., Xu, Y.H., Gai, H.F., et al., 2021b. Understanding water accessibility and pore information of over-mature marine shales using water vapor sorption. Mar. Petrol. Geol. 130, 105120. https://doi.org/10.1016/j.marpetgeo.2021.105120.
Chen, M.Y., Yang, Y.P., Gao, C.H., 2020. Investigation of the fractal characteristics of adsorption- pores and their impact on the methane adsorption capacity of various rank coals via N_2 and H_2O adsorption methods. Energy Sci. Eng. 8 (9), 3228–3243. https://doi.org/10.1002/ese3.727.
Cheng, M., Li, C., Zhou, L., et al., 2016. Marine Mo biogeochemistry in the context of dynamically euxinic mid-depth waters: a case study of the lower Cambrian Niutitang shales, South China. Geochem. Cosmochim. Acta 183 (1), 79–93. https://doi.org/10.1016/j.gca.2016.03.035.
Cheng, P., Tian, H., Xiao, X.M., et al., 2017. Water distribution in over-mature organic-rich shales: implications from water adsorption experiments. Energy Fuels 31 (12), 13120–13132. https://doi.org/10.1021/acs.energyfuels.7b01531.
Cheng, P., Xiao, X.M., Tian, H., et al., 2018. Water content and equilibrium saturation and their influencing factors of the lower paleozoic over-mature organic-rich shales in the Upper Yangtze Region of southern China. Energy Fuels 32 (11), 11452–11466. https://doi.org/10.1021/acs.energyfuels.8b03011.
Cheng, P., Xiao, X.M., Tian, H., et al., 2022. Differences in the distribution and occurrence phases of pore water in various nanopores of marine-terrestrial transitional shales in the Yangquan area of the northeast Qinshui Basin, China. Mar. Petrol. Geol. 137, 105510. https://doi.org/10.1016/j.marpetgeo.2021.105510.
Curtis, J.B., 2002. Fractured shale-gas systems. AAPG Bull. 86 (11), 1921–1938. https://doi.org/10.1306/61EEDDBE-173E-11D7-8645000102C1865D.
Curtis, M.E., Cardott, B.J., Sondergeld, C.H., et al., 2012. Development of organic porosity in the Woodford Shale with increasing thermal maturity. Int. J. Coal Geol. 103, 26–31. https://doi.org/10.1016/j.coal.2012.08.004.
Czepirski, L., Balys, M.R., Komorowska-Czepirska, E., 2000. Some generalization of Langmuir adsorption isotherm. Internet J. Chem. 3, 1099–8292. https://doi.org/10.2478/v10156-011-0033-8.
Dang, W., Jiang, S., Zhang, J.C., et al., 2021. A systematic experimental and modeling study of water adsorption/desorption behavior in organic-rich shale with different particle sizes. Chem. Eng. J. 426, 130596. https://doi.org/10.1016/j.cej.2021.130596.
Dent, R.W., 1977. A multilayer theory for gas sorption: Part I: sorption of a single gas. Textil. Res. J. 47 (2), 145–152. https://doi.org/10.1177/004051757704700213.
Dong, D.Z., Liang, F., Guan, Q.Z., et al., 2022. Development model and identification evaluation technology of WufengLongmaxi Formation quality shale gas reservoirs in the Sichuan Basin. Nat. Gas. Ind. 42 (8), 96–111. https://doi.org/10.3787/j.issn.1000-0976.2022.08.008 (in Chinese).
Dong, D.Z., Wang, Y.M., Li, X.J., et al., 2016. Breakthrough and prospect of shale gas exploration and development in China. Nat. Gas. Ind. 36 (1), 19–32. https://doi.org/10.3787/j.issn.1000-0976.2016.01.003 (in Chinese).
Donohue, M.D., Aranovich, G.L., 1998. Classification of Gibbs adsorption isotherms. Adv. Colloid Interface Sci. 77, 137–152. https://doi.org/10.1016/S0001-8686(98)00044-X.
Duan, S., Li, G.D., 2018. Equilibrium and kinetics of WVA on shale. J. Energy Resour. Technol. 140 (12), 122001. https://doi.org/10.1115/1.4040530.
Dubinin, M.M., 1989. Fundamentals of the theory of adsorption in micropores of carbon adsorbents: characteristics of their adsorption properties and microporous structures. Carbon 27 (3), 457–467. https://doi.org/10.1351/pac198961111841.
Fang, C.H., Huang, Z.L., Wang, Q.Z., et al., 2014. Cause and significance of the ultra-low water saturation in gas-enriched shale reservoir. Nat. Gas Geosci. 25 (3), 471–476. https://doi.org/10.11764/j.issn.1672-1926.2014.03.0471 (in Chinese).
Feng, D., Li, X.F., Wang, X.Z., et al., 2018. Water adsorption and its impact on the pore structure characteristics of shale clay. Appl. Clay Sci. 155, 126–138. https://doi.org/10.1351/pac198961111841.
Feng, Y., Xiao, X.M., Wang, E.Z., et al., 2023. Gas storage in shale pore system: a review of the mechanism, control and assessment. Petrol. Sci. 5, 2605–2636. https://doi.org/10.1016/j.petsci2023.05.012.
Gai, H.F., Tian, H., Cheng, P., et al., 2020. Characteristics of molecular nitrogen generation from over-mature black shales in South China: preliminary implications from pyrolysis experiments. Mar. Petrol. Geol. 120, 104527. https://doi.org/10.1016/j.marpetgeo.2020.104527.
Gao, P., Li, S.J., Lash, G.G., et al., 2021. Stratigraphic framework, redox history, and organic matter accumulation of an Early Cambrian intraplatfrom basin on the Yangtze Platform, South China. Mar. Petrol. Geol. 130, 105095. https://doi.org/10.1016/j.marpetgeo.2021.105095.
Gao, Z.Y., Xiong, S.L., Wei, L., 2022. The new multistage water adsorption model of Longmaxi Formation shale considering the spatial configuration relationship between organic matter and clay minerals. Petrol. Sci. 19 (5), 1950–1963. https://doi.org/10.1016/j.petsci.2022.05.014.
Gareth, R.C., Bustin, R.M., Power, I.M., 2012. Characterization of gas shale pore systems by porosimetry, pycnometry, surfacearea, and field emission scanning electron microscopy/transmission electron microscopy image analyses: examples from the Barnett, Woodford, Haynesville, Marcellus, and Doig units. AAPG Bull. 96 (6), 1099–1119. https://doi.org/10.1306/10171111052.
Ge, T.Y., Pan, J.N., Wang, K., et al., 2020. Heterogeneity of pore structure of late Paleozoic transitional facies coal-bearing shale in the Southern North China and its main controlling factors. Mar. Petrol. Geol. 122, 104710. https://doi.org/10.1016/j.marpetgeo.2020.104710.
Gregg, S.J., Sing, K.S.W., Salzberg, H.W., 1967. Adsorption surface area and porosity. J. Electrochem. 114 (11), 279Ca. https://doi.org/10.1149/1.2426447.
Guo, T.L., Zhang, H.R., 2014. Formation and enrichment mode of Jiaoshiba shale gas field, Sichuan Basin. Petrol. Explor. Dev. 41 (1), 28–36. https://doi.org/10.11698/PED.2014.01.03 (in Chinese).
Gu, X., Mildner, D.F.R., Cole, D.R., et al., 2016. Quantification of organic porosity and water accessibility in marcellus shale using neutron scattering. Energy Fuels 30 (6), 4438–4449. https://doi.org/10.1021/acs.energyfuels.5b02878.
Hagymassy, J., Brunauer, S., 1970. Pore structure analysis by WVA. II. Analysis of five silica gels. J. Colloid Interface Sci. 33 (2), 317. https://doi.org/10.1016/0021-9797(70)90035-4.
Hagymassy, J., Brunauer, S., Mikhail, R.F., 1969. Pore structure analysis by WVA: I. t-Curves for water vapor. J. Colloid Interface Sci. 29 (3), 485–491. https://doi.org/10.1016/0021-9797(69)90132-5.
Hao, F., Zou, H.Y., Lu, Y.C., 2013. Mechanisms of shale gas storage: implications for shale gas exploration in China. AAPG Bull. 97 (8), 1325–1346. https://doi.org/10.1306/02141312091.
Heller, R., Zoback, M., 2014. Adsorption of methane and carbon dioxide on gas shale and pure mineral samples. J. Unconv. 8, 14–24. https://doi.org/10.1016/j.juogr.2014.06.001.
Henry, D.G., Jarvis, I., Gillmore, G., et al., 2019. Raman spectroscopy as a tool to determine the thermal maturity of organic matter: application to sedimentary, metamorphic and structural geology. Earth Sci. Rev. 198, 102936. https://doi.org/10.1016/j.earscirev.2019.102936.
Hou, C.H., Yu, B.S., Liu, L., et al., 2021. Water uptake behavior and influence factors of Longmaxi Shale: implications from water physisorption and imbibition measurements. Energy Fuels 35 (15), 11958–11975. https://doi.org/10.1021/acs.energyfuels.1c01413.
Hou, L.H., Ma, W.J., Luo, X., et al., 2020. Chemical structure changes of lacustrine Type-II kerogen under semi-open pyrolysis as investigated by solid-state 13C NMR and FT-IR spectroscopy. Mar. Petrol. Geol. 116, 104348. https://doi.org/10.1016/j.marpetgeo.2020.104348.
Hou, Y.G., Zhang, K.P., Wang, F.R., et al., 2019. Structural evolution of organic matter and implications for graphitization in over-mature marine shales, south China. Mar. Petrol. Geol. 109, 304–316. https://doi.org/10.1016/j.marpetgeo.2019.06.009.
Hu, Y.N., Devegowda, D., Striolo, A., et al., 2015. Microscopic dynamics of water and hydrocarbon in shale-kerogen pores of potentially mixed wettability. SPE J. 20 (1), 112–124. https://doi.org/10.12118/167234-PA.
Hu, Y.N., Devegowda, D., Sigal, R., 2016. A microscopic characterization of wettability in shale kerogen with varying maturity levels. J. Nat. Gas Sci. Eng. 33, 1078–1086. https://doi.org/10.1016/j.jngse.2016.06.014.
Hu, Z.M., Duan, X.G., He, Y.B., et al., 2019. Influence of reservoir primary water on shale gas occurrence and flow capacity. Nat. Gas. Ind. B 6 (1), 71–78. https://doi.org/10.1016/j.ngib.2019.01.010.
Huang, J.L., Zou, C.N., Li, J.Z., et al., 2012. Shale gas generation and potential of the lower cambrian Qiongzhusi Formation in the southern Sichuan Basin, China. Petrol. Explor. Dev. 39 (1), 75–81. https://doi.org/10.1016/S1876-3804(12)60017-2.
Huang, Z.K., Liang, T., Zhan, Z.W., et al., 2018. Chemical structure evolution of kerogen during oil generation. Mar. Petrol. Geol. 98, 422–436. https://doi.org/10.1016/j.marpetgeo.2018.08.039.
Jiang, G.Q., Wang, X.Q., Shi, X.Y., et al., 2012. The origin of decoupled carbonate and organic carbon isotope signatures in the early Cambrian (ca. 542–520Ma) Yangtze platform. Earth Planet Sci. Lett. 317–318 (1), 96–110. https://doi.org/10.1016/j.epsl.2011.11.018.
Jiang, S., Wang, Y.M., Wang, S.Y., et al., 2018. Distribution prediction of graphitized organic matter areas in the Lower Cambrian Qiongzhusi shale in the Central Sichuan paleo-uplift and its surrounding areas in the Sichuan Basin. Nat. Gas. Ind. 38 (10), 19–27. https://doi.org/10.3787/j.issn.1000-0976.2018.10.003 (in Chinese).
Jin, Z.H., Firoozabadi, A., 2014. Effect of water on methane and carbon dioxide sorption in clay minerals by Monte Carlo simulations. Fluid Phase Equil. 382, 10–20. https://doi.org/10.1016/j.fluid.2014.07.035.
Kelemen, S.R., Fang, H.L., 2001. Maturity trends in Raman spectra from kerogen and coal. Energy Fuels 15 (3), 653–658. https://doi.org/10.1021/ef0002039.
Khan, H.J., Spielman, E., Jew, A.D., et al., 2021. A critical review of the physicochemical impacts of water chemistry on shale in hydraulic fracturing systems. Environ. Sci. Technol. 55 (3), 1377–1394. https://doi.org/10.1021/

acs.est.0c04901.
Korb, J.P., Nicot, B., Louis, A., et al., 2014. Dynamics and wettability of oil and water in oil shales. J. Phys. Chem. C 118 (40), 23212–23218. https://doi.org/10.1021/jp508659e.
Kozbial, A., Li, Z.T., Sun, J.N., et al., 2014. Understanding the intrinsic water wettability of graphite. Carbon 74, 218–225. https://doi.org/10.1016/j.carbon.2014.03.025.
Kuila, U., McCarty, D.K., Derkowski, A., et al., 2014. Nano-scale texture and porosity of organic matter and clay minerals in organic-rich mudrocks. Fuel 135, 359–373. https://doi.org/10.1016/j.fuel.2014.06.036.
Lahn, L., Bertier, P., Seemann, T., et al., 2020. Distribution of sorbed water in the pore network of mudstones assessed from physisorption measurements. Microporous Mesoporous Mater. 295, 109902. https://doi.org/10.1016/j.micromeso.2019.109902.
Li, G., Gao, P., Xiao, X.M., et al., 2022a. Lower cambrian organic-rich shales in southern China: a review of gas-bearing property, pore structure, and their controlling factors. Geofluids 1–23. https://doi.org/10.1155/2022/9745313.
Li, G., Xiao, X.M., Gai, H.F., et al., 2023a. Nanopore structures and controlling factors of the early cambrian shale reservoir in the middle Yangtze platform, south China. J. Asian Earth Sci. 254, 105738. https://doi.org/10.1016/j.jseaes.2023.105738.
Li, G., Xiao, X.M., Gai, H.F., et al., 2023b. Nanopore structure evolution of lower cambrian shale in the western hubei area, southern China, and its geological implications based on thermal simulation experimental results. Nat. Resour. Res. 32 (2), 731–754. https://doi.org/10.1007/s11053-022010149-1.
Li, J., Li, X.F., Wang, X.Z., et al., 2016. Water distribution characteristic and effect on methane adsorption capacity in shale clay. Int. J. Coal Geol. 159, 135–154. https://doi.org/10.1016/j.coal.2016.03.012.
Li, J.H., Li, B.B., Gao, Z., 2021a. WVA behavior in shale under different temperatures and pore structures. Nat. Resour. Res. 30 (3), 2789–2805. https://doi.org/10.1007/s11053-021-09846-0.
Li, J.Q., Wang, S.Y., Lu, S.F., et al., 2019a. Microdistribution and mobility of water in gas shale: a theoretical and experimental study. Mar. Petrol. Geol. 102, 496–507. https://doi.org/10.1016/j.marpetgeo.2019.01.012.
Li, T.F., Tian, H., Xiao, X.M., et al., 2020. The effect of particle size on low pressure gas adsorption experiments for highmaturity shale. Nat. Gas Geosci. 31 (9), 1271–1284. https://doi.org/10.11764/j.issn.1672-1926.2020.04.021 (in Chinese).
Li, W., Pang, X.Q., Snape, C., et al., 2019b. Molecular simulation study on methane adsorption capacity and mechanism in clay minerals: effect of clay type, pressure, and water saturation in shales. Energy Fuels 33, 765–778. https://doi.org/10.1021/acs.energyfuels.8b03462.
Li, W., Stevens, L.A., Uguna, C.N., et al., 2021b. Comparison of the impact of moisture on methane adsorption and nanoporosity for over mature shales and their kerogens. Int. J. Coal Geol. 237, 103705. https://doi.org/10.1016/j.coal.2021.103705.
Li, Y.J., Zhao, S.X., Huang, Y.B., et al., 2013. Study on sedimentary microfacies of lower cambrian Qiongzhusi Formation shale in southern Sichuan Basin. Acta Geol. Sin. 87 (8), 1136–1148 (in Chinese).
Li, Y.S., Liu, G.D., Song, Z.Z., et al., 2022b. Organic matter enrichment due to high primary productivity in the deep-water shelf: insights from the Lower Cambrian Qiongzhusi shales of the central Sichuan Basin, SW China. J. Asian Earth Sci. 239, 105417. https://doi.org/10.1016/j.jseaes.2022.105417.
Liang, Z.K., Jiang, Z.X., Han, Y.H., et al., 2023. A modified dent-fractal mathematical model to investigate the WVA on nanopore structure heterogeneity from the Longmaxi Shale, Sichuan Basin, China. Energy Fuels 37 (13), 9131–9150. https://doi.org/10.1021/acs.energyfuels.3c01171.
Liu, D.H., Xiao, X.M., Tian, H., et al., 2013. Sample maturation calculated using Raman spectroscopic parameters for solid organics: Methodology and geological applications. Chin. Sci. Bull. 58 (13), 1228–1241. https://doi.org/10.1007/s11434-012-5535-y (in Chinese).
Liu, H.L., Wang, H.Y., 2013. Ultra-low water saturation characteristics and the identification of over pressured play fairways of marine shales in south China. Nat. Gas. Ind. 33 (7), 140–144. https://doi.org/10.3787/j.issn.1000-0976.2013.07.025 (in Chinese).
Liu, S.B., Jin, S.D., Liu, Y., et al., 2022. Astronomical forced sequence infill of early Cambrian Qiongzhusi organic-rich shale of Sichuan Basin, South China. Sediment. Geol. 440, 106261. https://doi.org/10.1016/j.sedgeo.2022.106261.
Liu, Z.B., Gao, B., Zhang, Y.Y., et al., 2017. Types and distribution of the shale sedimentary facies of the lower cambrian in upper Yangtze area, south China. Petrol. Explor. Dev. 44 (1), 20–31. https://doi.org/10.1016/s1876-3804(17)30004-6.
Liubov, A.B., Pauline, M.G.D., Kassandra, I.B., 2018. Hydrophilicity of graphene in water through transparency to polar and dispersive interactions. Adv. Mater. 30 (6), 1703274. https://doi.org/10.1002/adma.201703274.
Llave, E.D.L., Molinero, V., Scherlis, D.A., 2012. Role of confinement and surface affinity on filling mechanisms and sorption hysteresis of water in nanopores. J. Phys. Chem. C 116 (2), 1833–1840. https://doi.org/10.1021/jp206580z.
Lu, C.G., Xiao, X.M., Gai, H.F., et al., 2023. Nanopore structure characteristics and evolution of type III kerogen in marine-continental transitional shales from the Qinshui basin, northern China. Geoenergy Science and Engineering 221, 211413. https://doi.org/10.1016/j.geoen.2022.211413.
Marin-Carbonne, J., Robert, F., Chaussidon, M., 2014. The silicon and oxygen isotope compositions of Precambrian cherts: a record of oceanic paleo-temperatures? Precambrian Res. 247, 223–234. https://doi.org/10.1016/j.precamres.2014.03.016.
Ma, Y., Zhong, N.N., Cheng, L.J., et al., 2015. Pore structure of two organic-rich shales in southeastern chongqing area: insight from focused ion beam scanning electron microscope (FIB-SEM). Petrol. Geosci. 37 (1), 109–116. https://doi.org/10.11781/sysydz201501109 (in Chinese).
McCutcheon, A.L., Barton, W.A., 1999. Contribution of mineral matter to water associated with bituminous coals. Energy Fuels 13 (1), 160–165. https://doi.org/10.1021/ef980151b.
Nie, H.K., Li, P., Dang, W., et al., 2022. Enrichment characteristics and exploration directions of deep shale gas of Ordovician-Silurian in the Sichuan Basin and its surrounding areas, China. Pet. Explor. Dev. 49 (4), 648–659. https://doi.org/10.11698/PED.20210882 (in Chinese).
Nie, H.K., Tang, X., Bian, R.K., 2009. Controlling factors for shale gas accumulation and prediction of potential development area in shale gas reservoir of South China. Acta Petrol. Sin. 30 (4), 484–491 (in Chinese).
Odusina, E., Sondergeld, C., Rai, C., 2011. An NMR study on shale wettability. Canadian Unconventional Resources Conference. https://doi.org/10.2118/147371-MS.
Osipov, V.I., 2012. Nanofilms of adsorbed water in clay: mechanism of formation and properties. Water Resour. 39 (7), 709–721. https://doi.org/10.1134/S009780781207010X.
Parmar, J.S., Dehghanpour, H., Kuru, E., 2013. Drainage against gravity: factors impacting the load recovery in fractures. In: SPE Unconventional Resources Conference-USA. https://doi.org/10.2118/164530-MS.
Passey, Q.R., Bohacs, K.M., Esch, W.L., et al., 2010. From oil-prone source rock to gas-producing shale reservoir-geologic and petrophysical characterization of unconventional shale-gas reservoirs. In: International Oil and Gas Conference and Exhibition in China. https://doi.org/10.2118/131350-MS.
Pecharesky, V.K., Zavalij, P.Y., 2005. Fundamentals of powder diffraction and structural characterization of materials. Chem. Aust. 72 (10), 31. https://doi.org/10.1007/978-0-387-09579-0.
Pi, D.H., Liu, C.Q., Shields-Zhou, G.A., et al., 2013. Trace and rare earth element geochemistry of black shale and kerogen in the early Cambrian Niutitang Formation in Guizhou province, South China: constraints for redox environments and origin of metal enrichments. Precambrian Res. 225, 218–229. https://doi.org/10.1016/j.precamres.2011.07.004.
Quirico, E., Rouzaud, J., Bonal, L., et al., 2005. Maturation grade of coals as revealed by Raman spectroscopy: progress and problems. Spectrochim. Acta 61A (10), 2368–2377. https://doi.org/10.1016/j.saa.2005.02.015.
Rao, S., Yang, Y.N., Hu, S.B., et al., 2022. Thermal evolution history and shale gas accumulation significance of lower cambrian Qiongzhusi Formation in southwest Sichuan Basin. Earth Sci. 47 (11), 4319–4335. https://doi.org/10.3799/dqkx.2022.153 (in Chinese).
Ren, D.C., Chen, Y.C., Sun, C.Y., et al., 2016. Shale gas reservoir-forming conditions and predicting favorable exploration area in Qiongzhusi formation, Vying region. Petrochemical Industry Application 35 (8), 99–103. https://doi.org/10.3969/j.issn.1673-5285.2016.08.022 (in Chinese).
Ren, D.C., Wang, X.F., Liu, X.D., et al., 2017. Evaluation criterion and favorable exploration block forecast in Qiongzhusi Formation of weiyuan area. Unconventional Oil & Gas 4 (5), 38–43 (in Chinese).
Ren, W.X., Guo, J.C., Zeng, F.H., et al., 2019. Modeling of high-pressure methane adsorption on wet shales. Energy Fuels 33 (8), 7043–7051. https://doi.org/10.1021/acs.energyfuels.9b01024.
Sang, G.J., Liu, S.M., Elsworth, D., 2019. Water vapor sorption properties of Illinois shales under dynamic water vapor conditions: experimentation and modeling. Water Resour. Res. 55 (8), 7212–7228. https://doi.org/10.1029/2019WR024992.
Sang, G.J., Liu, S.M., Elsworth, D., et al., 2020. Evaluation and modeling of water vapor sorption and transport in nanoporous shale. Int. J. Coal Geol. 228, 103553. https://doi.org/10.1016/j.coal.2020.103553.
Sang, G.J., Liu, S.M., Zhang, R., et al., 2018. Nanopore characterization of mine roof shales by SANS, nitrogen adsorption, and mercury intrusion: impact on water adsorption/retention behavior. Int. J. Coal Geol. 200, 173–185. https://doi.org/10.1016/j.coal.2018.11.009.
Shen, C.B., Mei, L.F., Xu, Z.P., et al., 2007. Structural structure and evolution of compound basin-mountain system in Sichuan Basin. Geotectonics and Metallogeny 31 (3), 288–299. https://doi.org/10.16539/j.ddgzyckx.2007.03.002 (in Chinese).
Shen, W.J., Li, X.Z., Lu, X.B., et al., 2018. Experimental study and isotherm models of WVA in shale rocks. J. Nat. Gas Sci. Eng. 52, 484–491. https://doi.org/10.1016/j.jngse.2018.02.002.
Shi, K.Y., Chen, J.Q., Pang, X.Q., et al., 2023. Wettability of different clay mineral surfaces in shale: implications from molecular dynamics simulations. Petrol. Sci. 20, 689–704. https://doi.org/10.1016/j.petsci.2023.02.001.
Sing, K.S.W., Ecerett, D.H., Haul, R.A.W., et al., 1985. Reporting physisorption data for gas/solid systems with special reference to the determination of surface area and porosity. Pure Appl. Chem. 57 (4), 603–619. https://doi.org/10.1351/pac198557040603.
Sing, K.S.W., Williams, R.T., 2004. Physisorption hysteresis loops and the characterization of nanoporous materials. Adsorpt. Sci. Technol. 22 (10), 773–782. https://doi.org/10.1260/0263617053499032.
Sing, K.S.W., Rouquerol, F., Rouquerol, J., 2012. 5-Classical interpretation of physisorption isotherms at the gas–solid interface. Adsorption by Powders and Porous Solids, second ed., pp. 159–189. https://doi.org/10.1016/B978-0-08-097035-6.00005-X
Sondergeld, C.H., Newsham, K.E., Comisky, J.T., et al., 2010. Petrophysical Considerations in Evaluating and Producing Shale Gas Resources. SPE Unconventional

Gas Conference.
Song, X., Chen, C., Arthur, E., et al., 2022. Cation exchange capacity and soil pore system play key roles in water vapour sorption. Geoderma 424, 116017. https://doi.org/10.1016/j.geoderma.2022.116017.
Song, Z.Z., Abide, A., Lv, Y.M., et al., 2023. Quantitative analysis of nitrogen adsorption hysteresis loop and its indicative significance to pore structure characterization:A case study on the Upper Triassic Chang 7 Member, Ordos Basin. Oil Gas Geol. 44 (2), 495–509. https://doi.org/10.11743/ogg20230219 (in Chinese).
Sui, Q.L., 2017. Micro heterogeneity of jiulaodong Formation shale, weiyuan area. Sichuan. Fault-Block Oil & Gas Field. 24 (1), 15–20. https://doi.org/10.6056/dkyqt201701004 (in Chinese).
Suleimenova, A., Bake, K.D., Ozkan, A., et al., 2014. Acid demineralization with critical point drying: a method for kerogen isolation that preserves microstructure. Fuel 135, 492–497. https://doi.org/10.1016/j.fuel.2014.07.005.
Sun, J., Xiao, X.M., Wei, Q., et al., 2021. Occurrence of irreducible water and its influences on gas-bearing property of gas shales from shallow Longmaxi Formation in the xishui area, guizhou, southern China. Front. Earth Sci. 9, 654136. https://doi.org/10.3389/feart.2021.654136.
Švábová, M., Weishauptová, Z., Přibyl, O., 2011. Water vapour adsorption on coal. Fuel 90 (5), 1892–1899. https://doi.org/10.1016/j.fuel.2011.01.005.
Tang, X., Ripepi, N., Valentine, K.A., et al., 2017. Water vapor sorption on Marcellus shale: measurement, modeling and thermodynamic analysis. Fuel 209 (1), 606–614. https://doi.org/10.1016/j.fuel.2017.07.062.
Tatzel, M., Blanckenburg, F.V., Oelze, M., et al., 2017. Late Neoproterozoic seawater oxygenation by siliceous sponges. Nat. Commun. 8 (1), 621. https://doi.org/10.1038/s41467-017-00586-5.
Thommes, M., Kaneko, K., Neimark, A.V., et al., 2015. Physisorption of gases, with special reference to the evaluation of surface area and pore size distribution (IUPAC Technical Report). Pure Appl. Chem. 87, 1051–1069. https://doi.org/10.1515/pac-2014-1117, 9–10.
Tian, H., Pan, L., Xiao, X.M., et al., 2013. A preliminary study on the pore characterization of Lower Silurian black shales in the Chuandong Thrust Fold Belt, southwestern China using low pressure N_2 adsorption and FE-SEM methods. Mar. Petrol. Geol. 48, 8–19. https://doi.org/10.1016/j.marpetgeo.2013.07.008.
Tian, H., Pan, L., Zhang, T.W., et al., 2015. Pore characterization of organic-rich lower cambrian shales in qiannan depression of guizhou province, southwestern China. Mar. Petrol. Geol. 62, 28–43. https://doi.org/10.1016/j.marpetgeo.2015.01.004.
Tian, X.W., Hu, G.Y., Su, G.P., et al., 2018. Mineralogical characteristics of paleozoic marine shales in well W201 of weiyuan area, southern Sichuan Basin. Xinjing Pet. Geol. 39 (4), 409–415. https://doi.org/10.7657/XJPG20180405 (in Chinese).
Ukaomah, C.F., Sun, M.D., Pan, Z.J., et al., 2023. Experimental and molecular investigation of water adsorption controls in marine and lacustrine shale reservoirs. J. Hydrol. 621, 129672. https://doi.org/10.1016/j.jhydrol.2023.129672.
Wan, K.J., He, Q.Q., Miao, Z.Y., et al., 2016. Water desorption isotherms and net isosteric heat of desorption on lignite. Fuel 171, 101–107. https://doi.org/10.1016/j.fuel.2015.12.054.
Wang, D.F., Wang, Y.M., Dong, D.Z., et al., 2013a. Quantitative characterization of reservoir spaceinthe lower cambrian Qiongzhusi shale, southern Sichuan Basin. Nat. Gas. Ind. 33 (7), 1–10. https://doi.org/10.3787/j.issn.1000-0976.2013.07.001 (in Chinese).
Wang, H.Y., Liu, Y.Z., Dong, D.Z., et al., 2013b. Scientific issues on effective development of marine shale gas in southern China. Petrol. Explor. Dev. 40 (5), 615–620. https://doi.org/10.1016/S1876-3804(13)60080-4.
Wang, L.S., Zou, C.Y., Zheng, P., et al., 2009. Geochemical basis of shale gas in lower paleozoic in lower paleozoic in Sichuan Basin. Nat. Gas. Ind. 29 (5), 59–62. https://doi.org/10.3787/j.issn.1000–0976.2009.05.011 (in Chinese).
Wang, M., Lun, Z.M., Zhao, C.P., et al., 2020a. Influences of primary moisture on methane adsorption within lower silurian Longmaxi shales in the Sichuan Basin, China. Energy Fuels 34 (9), 10810–10824. https://doi.org/10.1021/acs.energyfuels.0c01932.
Wang, M.L., Xiao, X.M., Wei, Q., et al., 2015. Thermal maturation of solid bitumen in shale as revealed by Raman spectroscopy. Nat. Gas Geosci. 26 (9), 1712–1718. https://doi.org/10.11764/j.issn.1672–1926.2015.09.1712 (in Chinese).
Wang, P.F., Yao, S.Q., Jin, C., et al., 2020b. Key reservoir parameter for effective exploration and development of high-over matured marine shales: a case study from the cambrian Niutitang formation and the silurian Longmaxi formation, south China. Mar. Petrol. Geol. 121, 104619. https://doi.org/10.1016/j.marpetgeo.2020.104619.
Wang, P.W., Liu, Z.B., Jin, Z.J., et al., 2019a. Main control factors of shale gas differential vertical enrichment in lower cambrian Qiongzhusi Formation, southwest Sichuan Basin, China. Earth Sci. 44 (11), 3628–3638. https://doi.org/10.3799/dqkx.2019.183 (in Chinese).
Wang, R.Y., Hu, Z.Q., Nie, H.K., et al., 2018. Comparative analysis and discussion of shale reservoir characteristics in the Wufeng-Longmaxi and Niutitang formations. Petrol. Geosci. 40 (5), 639–649. https://doi.org/10.11781/sysydz201805639 (in Chinese).
Wang, T.Y., Tian, S.C., Li, G.S., et al., 2019b. Experimental study of WVA behaviors on shale. Fuel 248, 168–177. https://doi.org/10.1016/j.fuel.2019.03.029.
Wang, Y.F., Leng, J.G., Li, P., et al., 2016a. Characteristics and its main enrichment controlling factors of shale gas of the Lower Cambrian Niutitang Formation in northeastern Guizhou Province. J. Palaeogeogr. 18 (4), 605–614. https://doi.org/10.1605/gdlxb.2016.04.045 (in Chinese).
Wang, Y.M., Dong, D.Z., Cheng, X.Z., et al., 2014. Electric property evidences of the carbonification of organic matters in marine shales and its geologic significance: a case of the Lower Cambrian Qiongzhusi Shale in southern Sichuan Basin. Nat. Gas. Ind. 34 (8), 1–7. https://doi.org/10.3787/j.issn.1000–0976.2014.08.001 (in Chinese).
Wang, Y.M., Li, J.X., 2018. Lower limit of thermal maturity for the carbonization of organic matter in marine shale and its exploration risk. Petrol Explr Dev 45 (3), 385–395. https://doi.org/10.11698/PED.2018.03.03 (in Chinese).
Wang, Z., Li, X.Q., Zhou, B.G., et al., 2016b. Characterization of microscopic pore structure and its influence on gas content of shale gas reservoirs from the Lower Paleozoic in southern Sichuan Basin. J. China Coal Soc. 41 (9), 2287–2297. https://doi.org/10.13225/j.cnki.Jccs.2016.0425 (in Chinese).
Wang, Y., Qiu, N.S., Xie, X.M., et al., 2021. Maturity and thermal evolution differences between two sets of Lower Palaeozoic shales and its significance for shale gas formation in south-western Sichuan Basin, China. Geol. J. 56 (7), 1–22. https://doi.org/10.1002/gj.4121.
Wei, Y.Y., Jia, C.Q., 2015. Intrinsic wettability of graphitic carbon. Carbon 87, 10–17. https://doi.org/10.1016/j.carbon.2015.02.019.
Wu, K.L., Chen, Z.X., Li, X.F., et al., 2017. Flow behavior of gas confined in nanoporous shale at high pressure: real gas effect. Fuel 205, 173–183. https://doi.org/10.1021/j.fuel.2017.05.055.
Xiang, J., Zhu, Y.M., Wang, Y., et al., 2024. Deformation and kerogen macromolecular structure transformations of the Wufeng–Longmaxi shale under the control of the detachment layer. Mar. Petrol. Geol. 161, 106689. https://doi.org/10.1016/j.marpetgeo.2024.
Xiao, X.M., Wei, Q., Gai, H.F., et al., 2015. Main controlling factors and enrichment area evaluation of shale gas of the Lower Paleozoic marine strata in south China. Petrol. Sci. 12 (4), 573–586. https://doi.org/10.1007/s12182–015–0057–2.
Xie, W.D., Wang, H., Chen, S., et al., 2023. Water adsorption and its pore structure dependence in shale gas reservoirs. Langmuir 39 (30), 10576–10592. https://doi.org/10.1021/acs.langmuir.3c01159.
Xing, Y.J., Xiao, X.M., Zhao, Y.M., et al., 2024. Thermodynamic and kinetic behaviors of water vapor adsorption on the lower Cambrian over-mature shale and kerogen. Fuel 381, 133560. https://doi.org/10.1016/j.fuel.2024.133560.
Xing, Y.J., Xiao, X.M., Zhou, Q., et al., 2023. Influence of water on the methane adsorption capacity of organic-rich shales and its controlling factors: a review. Energies 16, 3305. https://doi.org/10.3390/en16083305.
Xiong, S.L., Chen, M.F., Yu, H., et al., 2023. Experimental investigation of thermodynamic and kinetic behaviors from WVA on four typical clay minerals. J. Nat. Gas Sci. Eng. 111, 204933. https://doi.org/10.1016/j.jgsce.2023.204933.
Xu, L.W., Wei, H., Chen, L., et al., 2022. Storing characteristics and main controlling factors of connate water in lower Paleozoic shales in southeast Chongqing, China. J. Petrol. Sci. Eng. 215 (Part B), 110543. https://doi.org/10.1016/j.petrol.2022.110543.
Xu, R., Prodanović, M., Landry, C., 2020. Pore scale study of gas sorption hysteresis in shale nanopores using lattice Boltzmann method. Int. J. Coal Geol. 229, 103568. https://doi.org/10.1016/j.coal.2020.103568.
Xu, R., Prodanović, M., 2018. Effect of pore geometry on nitrogen sorption isotherms interpretation: a pore network modeling study. Fuel 225, 243–255. https://doi.org/10.1016/j.fuel.2018.03.143.
Xu, Z., Shi, W.Z., Zhai, G.Y., et al., 2017. Relationship differences and causes between porosity and organic carbon in black shales of the Lower Cambrian and the Lower Silurian in Yangtze Area. Earth Sci. 42 (2), 1223–1234. https://doi.org/10.3799/dqkx.2017.099 (in Chinese).
Xu, Z.Y., Jiang, S., Yao, G.S., et al., 2019. Tectonic and depositional setting of the lower Cambrian and lower Silurian marine shales in the Yangtze Platform, South China: implications for shale gas exploration and production. J. Asian Earth Sci. 170, 1–19. https://doi.org/10.1016/j.jseaes.2018.10.023.
Yan, J.F., Men, Y.P., Sun, Y.Y., et al., 2016. Geochemical and geological characteristics of the Lower Cambrian shales in the middle-upper Yangtze area of South China and their implication for the shale gas exploration. Mar. Petrol. Geol. 70, 1–13. https://doi.org/10.1016/j.marpetgeo.2015.11.010.
Yang, R., Jia, A.Q., He, S., et al., 2020a. Water adsorption characteristics of organic-rich Wufeng and Longmaxi shales, Sichuan Basin (China). J. Petrol. Sci. Eng. 193, 107387. https://doi.org/10.1016/j.petrol.2020.107387.
Yang, R., Jia, A.Q., He, S., et al., 2021. Experimental investigation of WVA isotherm on gas-producing Longmaxi shale: mathematical modeling and implication for water distribution in shale reservoirs. Chem. Eng. J. 406, 125982. https://doi.org/10.1016/j.cej.2020.125982.
Yang, R., Jia, A.Q., Hu, Q.H., et al., 2020b. Particle size effect on water vapor sorption measurement of organic shale: one example from dongyuemiao member of lower jurassic Ziliujing Formation in Jiannan area of China. Advances in Geo-Energy Research 4 (2), 207–218. https://doi.org/10.26804/ager.2020.02.09.
Yang, W., Zuo, R.S., Jiang, Z.X., et al., 2018. Effect of lithofacies on pore structure and new insights into pore-preserving mechanisms of the over-mature Qiongzhusi marine shales in Lower Cambrian of the southern Sichuan Basin, China. Mar. Petrol. Geol. 98, 746–762. https://doi.org/10.1016/j.marpetgeo.2018.09.020.
Yang, Y., Wang, H., Xie, J.R., et al., 2023. Exploration breakthrough and prospect of

permian marine shale gas in the kaijiang-liangping trough, Sichuan Basin. Nat. Gas. Ind. 43 (11), 19–27. https://doi.org/10.3787/j.issn.1000-0976.2023.11.003 (in Chinese).

You, L.J., Zhang, N., Kang, Y.L., et al., 2021. Zero flowback rate of hydraulic fracturing fluid in shale gas reservoirs: concept, feasibility, and significance. Energy Fuels 35 (7), 5671–5682. https://doi.org/10.1021/acs.energyfuels.1c00232.

Yu, L.J., Liu, K.Y., Fan, M., et al., 2021. Co-occurring characteristics of pore gas and water in shales:a case study of the Lower Silurian Longmaxi Formation in the southeastern Sichuan Basin. Petrol. Geosci. 43 (6), 1089–1096. https://doi.org/10.11781/sysydz2021061089 (in Chinese).

Zhang, C., Yao, Y.B., Swennen, R., et al., 2022a. Combined effects of the chemical structure and nanopore development on water vapor/liquid adsorption in shale kerogen. Colloids & Surfaces A. Phys. Eng. Asp. 653, 129920. https://doi.org/10.1016/j.colsurfa.2022.129920.

Zhang, J.C., Jia, K.C., Huang, Y.F., et al., 2022b. Intrinsic wettability in pristine graphene. Adv. Mater. 34 (6), 2103620. https://doi.org/10.1002/adma.202103620, 1–8.

Zhang, K., Jia, C.Z., Song, Y., et al., 2019. Analysis of Lower Cambrian shale gas composition, source and accumulation pattern in different tectonic backgrounds: a case study of Weiyuan Block in the Upper Yangtze region and Xiuwu Basin in the Lower Yangtze region. Fuel 263, 115978. https://doi.org/10.1016/j.fuel.2019.115978.

Zhang, T.W., Luo, H., Meng, K., 2023. Main factors controlling the shale gas content of Cambrian shales of southern China-a discussion. Earth Sci. Front. 30 (3), 1–13. https://doi.org/10.13745/j.esf.sf.2022.5.31 (in Chinese).

Zhang, Y.F., Yu, B.S., Pan, Z.J., et al., 2020. Effect of thermal maturity on shale pore structure: a combined study using extracted organic matter and bulk shale from Sichuan Basin, China. J. Nat. Gas Sci. Eng. 74, 103089. https://doi.org/10.1016/j.jngse.2019.103089.

Zhang, Y., Hui, D., Zhang, J., et al., 2022c. Characteristics and main controlling factors of WVA in marine shale: a case study of the Lower Silurian Longmaxi shales in southern Sichuan Basin. Oil Gas Geol. 43 (6), 1431–1444. https://doi.org/10.11743/ogg20220612 (in Chinese).

Zhao, J.H., Jin, Z.J., Hu, Q.H., et al., 2019. Geological controls on the accumulation of shale gas: a case study of the early Cambrian shale in the Upper Yangtze area. Mar. Petrol. Geol. 107, 423–437. https://doi.org/10.1016/j.marpetgeo.2019.05.014.

Zhao, W.Z., Li, J.Z., Yang, T., et al., 2016. Geological difference and its significance of marine shale gases in South China. Petrol. Explor. Dev. 43 (4), 547–559. https://doi.org/10.1016/S1876-3804(16)30065-9.

Zhou, Q., Xiao, X.M., Tian, H., et al., 2014. Modeling free gas content of the lower paleozoic shales in the weiyuan area of the Sichuan Basin, China(article). Mar. Petrol. Geol. 56, 87–96. https://doi.org/10.1016/j.marpetgeo.2014.04.001.

Zhu, H.J., Ju, Y.W., Huang, C., et al., 2020. Microcosmic gas adsorption mechanism on clay-organic nanocomposites in a marine shale. Energy 197, 117256. https://doi.org/10.1016/j.energy.2020.117256.

Zolfaghari, A., Dehghanpour, H., Holyk, J., 2017a. Water sorption behaviour of gas shales: I. Role of clays. Int. J. Coal Geol. 179, 130–138. https://doi.org/10.1016/j.coal.2017.05.008.

Zolfaghari, A., Dehghanpour, H., Xu, M.X., 2017b. Water sorption behaviour of gas shales: II. Pore size distribution. Int. J. Coal Geol. 179, 187–195. https://doi.org/10.1016/j.coal.2017.05.009.

Zou, C.N., Yang, Z., Zhu, R.K., et al., 2015. Progress in China's unconventional oil & gas exploration and development and theoretical technologies. Acta Geol Sin-Engl 89 (3), 938–971. https://doi.org/10.1111/1755–6724.12491 (in Chinese).